

Search for the radiative decays of $\psi(3770) \rightarrow \gamma\eta_c(1S, 2S)$

Chi Zhang^{1,2} *, Jingzhi Zhang², Shenjian Chen¹

¹School of Physics, Nanjing University, Nanjing 210093, P. R. China

²Institute of High Energy Physics, Academy of Sciences, Beijing 100049, P.R. China

BESIII Analysis Memo (BAM-00094): Version 5.0

January 18, 2014

Abstract

By analyzing a 2.92 fb^{-1} data sample taken at $\sqrt{s} = 3.773 \text{ GeV}$ with the BES-III detector at the BEPC-II collider during 2010 and 2011, we search for the radiative transition between $\psi(3770)$ and η_c , $\eta_c(2S)$ through the hadronic final states $\eta_c(\eta_c(2S)) \rightarrow K_S^0 K^\pm \pi^\mp$ for the first time. Since no significant excess of signal events above the background is observed, we set the upper limits at 90% C.L. for the product branching fractions $\mathcal{B}(\psi(3770) \rightarrow \gamma\eta_c) \times \mathcal{B}(\eta_c \rightarrow K_S^0 K^\pm \pi^\mp) < 1.6 \times 10^{-5}$, $\mathcal{B}(\psi(3770) \rightarrow \gamma\eta_c(2S)) \times \mathcal{B}(\eta_c(2S) \rightarrow K_S^0 K^\pm \pi^\mp) < 5.8 \times 10^{-6}$, and the branching fractions $\mathcal{B}(\psi(3770) \rightarrow \gamma\eta_c) < 6.9 \times 10^{-4}$, $\mathcal{B}(\psi(3770) \rightarrow \gamma\eta_c(2S)) < 2.1 \times 10^{-3}$.

*Email: zhangchi@ihep.ac.cn

Contents

1	Introduction	3
2	The BEPCII and BESIII detector	5
3	Data sets and MC simulation	6
3.1	Data sets	6
3.2	Software framework and MC simulation	6
4	General event selection	7
4.1	Good photon selection	7
4.2	K_S^0 selection	7
4.3	Good charged track selection	9
4.4	Kinematic fit	9
4.5	Particle identification	9
5	Background suppression	9
5.1	4C kinematic fit	9
5.2	D^0 events rejection (D^0 veto)	11
5.3	π^0 events rejection (π^0 veto)	11
5.4	Cut flow and reconstruction efficiency	11
5.5	MC and data comparison	13
6	Measurement of $\psi(3770) \rightarrow \gamma\eta_c$, $\eta_c \rightarrow K_S^0 K^\pm \pi^\mp$	15
6.1	Background study	15
6.1.1	Backgrounds estimated by the inclusive MC samples	15
6.1.2	Background from $\pi^0 K_S^0 K^\pm \pi^\mp$	15
6.1.3	Background from $K_S^0 K^\pm \pi^\mp (\gamma_{ISR}/\gamma_{FSR})$	16
6.1.4	Background from $\psi(3686)$ tail	18
6.1.5	Potential peaking background check	19
6.2	Mass spectrum fitting results of real data	19
6.2.1	The detector resolution	19
6.2.2	Fit to the mass spectrum	19
6.2.3	Input/Output check	23
7	Measurement of $\psi(3770) \rightarrow \gamma\eta_c(2S)$, $\eta_c(2S) \rightarrow K_S^0 K^\pm \pi^\mp$	25
7.1	Background study	25
7.1.1	Backgrounds estimated by the inclusive MC samples	25
7.1.2	Background from $\pi^0 K_S^0 K^\pm \pi^\mp$	26
7.1.3	Background from $K_S^0 K^\pm \pi^\mp (\gamma_{ISR}/\gamma_{FSR})$	27
7.1.4	Background from $\psi(3686)$ tail	27
7.1.5	Potential peaking background check	28
7.2	Mass spectrum fitting results of real data	29
7.2.1	The detector resolution	29
7.2.2	Fit to the mass spectrum	29
7.2.3	Input/Output check	33

8 Systematic uncertainties	34
8.1 Tracking efficiency for π , K from IP	34
8.2 Photon detection efficiency	34
8.3 Efficiency for K_S^0 reconstruction	34
8.4 Efficiency for χ^2 cut of kinematic fitting	36
8.5 Efficiency for D^0 and π^0 veto	37
8.6 Integrated luminosity of data	37
8.7 Cross section of $\psi(3770)$	37
8.8 Possible intermediate states	39
8.9 Fitting in η_c & J/ψ mass region	39
8.10 Fitting in χ_{c1} & $\eta_c(2S)$ mass region	40
8.11 Background from $\psi(3686)$ tail	41
8.12 Total systematic error	41
9 Results and discussion	42
References	44
Appendix	46
A Calculation of the ISR resonances cross sections	46

1 Introduction

Charmonium spectrum and decays are an ideal place for studying the strong interaction dynamics in the interplay of perturbative and non-perturbative QCD regime. In the past decades there have been significant progresses made on the measurement of charmonium spectrum and their decays, which provide important constraints on phenomenological approaches. Figure 1 shows the spectrum of the charmonia and the observed transitions among them.

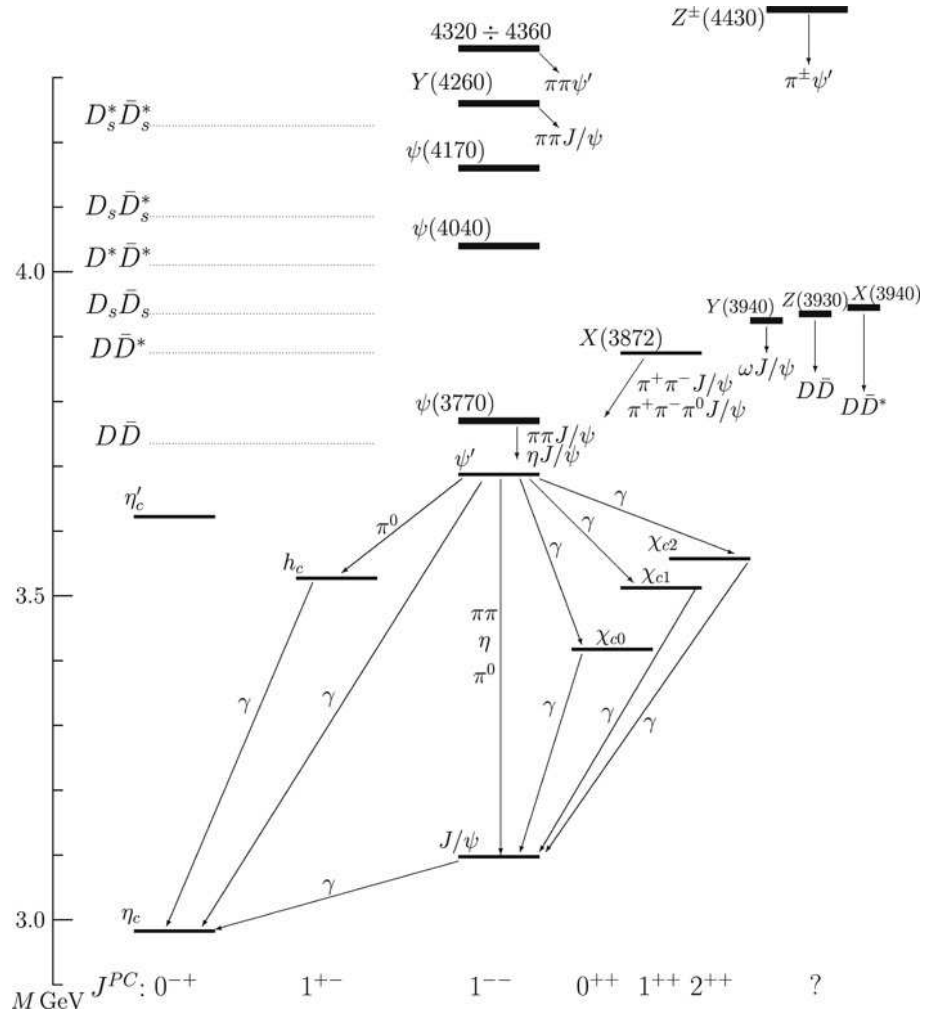


Figure 1: The known charmonium and charmonium-related resonances and some transitions between them. Also shown (dotted lines) are the thresholds for various pairs charmed mesons.

As the first charmonium state discovered in the history, J/ψ has been one of the most widely studied states in both experiment and theory. As a relatively heavier system compared with light $q\bar{q}$ mesons, the application of a nonrelativistic potential model (NR model) including color Coulomb plus linear scalar potential and spin-spin, spin-orbit interactions, has provided a reasonably good prescription for the charmonium spectrum [1]. This success is a direct indication of the validity of the naive “quenched” $c\bar{c}$ quark model scenario as a leading approximation in many circumstances. A relativised version was developed by Godfrey and Isgur [2] (GI model), where a flavor-dependent potential and QCD-motivated running coupling are employed. In comparison with the nonrelativistic model, the GI model offers a reasonably good description

of the spectrum and matrix elements of most of the u, d, s, c and b quarkonia [2, 3].

However, there also arise apparent deviations in the spectrum observables which give warnings to a simple $q\bar{q}$ treatment. A well-known problem is evident that both NR and GI model have predicted relatively larger branching ratios for J/ψ and $\psi' \rightarrow \gamma\eta_c(\gamma\eta_c(2S))$. In particular, the predicted partial decay width for $\psi' \rightarrow \gamma\eta_c$ was nearly 1 order of magnitude larger than the experimental data. So, more complicated mechanisms may play a role. As pointed out in Ref. [3], the importance of mixing between quark model $q\bar{q}$ states and two meson continua may produce significant effects in the spectrum observables. By including the meson loops, the quark model is practically “unquenched”. This immediately raises questions about the range of validity of the naive “quenched” $q\bar{q}$ quark model scenario, and the manifestations of the intermediate meson loops in charmonium spectrum and their decays. These issues become an interesting topic in the study of charmonium spectrum with high-statistic charmonium events from experiment.

$\psi(3770)$ resonance is believed to be a mixture of the 1^3D_1 and 2^3S_1 states of the $c\bar{c}$ system. Since its mass is above the open charm-pair threshold and its width is two orders of magnitude larger than that of $\psi(3686)$, it is thought to decay almost entirely to pure $D\bar{D}$ final states before 2003. During the time period from 2003 to 2008, the BES-II collaboration made extended studies of $\psi(3770)$ production and decays. In 2003, they observed the first non- $D\bar{D}$ decay mode of the particle of mass lying above the $D\bar{D}$ production energy threshold, $\psi(3770) \rightarrow J/\psi\pi^+\pi^-$, and they made the first measurement of the non- $D\bar{D}$ decay branching fraction of $\psi(3770)$. By analyzing different data sets taken at 3.773 GeV and 3.65 GeV as well as taken at more than 70 different energy points in the range from 3.65 to 3.89 GeV, BES-II collaboration measured the branching fractions for $\psi(3770)$ decays to inclusive non- $D\bar{D}$ final states to be $(14.7 \pm 3.2)\%$ [4, 5, 6, 7]. In 2005, the CLEO collaboration confirmed the BES-II observation of $\psi(3770) \rightarrow J/\psi\pi^+\pi^-$ and they observed the decays of $\psi(3770) \rightarrow \gamma\chi_{cJ(J=0,1)}$. The large inclusive non- $D\bar{D}$ branching fraction for $\psi(3770)$ decays may indicate that there are some effects we still don't understand very well about the traditional resonance(s) lying above the $D\bar{D}$ threshold. Measurement of the branching fractions or partial widths for $\psi(3770)$ decays to non- $D\bar{D}$ final states can help us to understand the nature of the traditional $\psi(3770)$ better.

Charmonium states that are above the ground state can have significant decays into the states with lower mass that proceed via electromagnetic transitions. For the $\psi(3770)$ resonance, although it predominantly decays to $D\bar{D}$ final states, there are, in addition, electromagnetic transitions between the $\psi(3770)$ and lower mass states. For $\psi(3770) \rightarrow \gamma\eta_c(\eta_c(2S))$, if $\psi(3770)$ is a pure D-wave state, the M1 transition will be forbidden by the selection rule of Eq. 1:

$$\Gamma_{M1}(n^{2S+1}L_J \rightarrow n'^{2S'+1}L'_{J'} + \gamma) = \frac{4(2J'+1)}{3(2J+1)} \delta_{LL'} \delta_{S,S'+1} \frac{e_c^2 \alpha}{m_c^2} |\langle \psi_f | \psi_i \rangle|^2 E_\gamma^3 \frac{E_f}{M_i}, \quad (1)$$

where $n(n')$, $S(S')$, $L(L')$, $J(J')$, $|\psi_i\rangle(|\psi_f\rangle)$ are the initial(final) state main quantum number, spin, orbital angular momentum, total angular momentum, and spatial wave functions, respectively. E_γ and E_f denote the final state photon and meson energy, respectively, while M_i is the initial $c\bar{c}$ meson mass. However, due to the nonvanishing photon energy in the decay, higher multipoles beyond the leading one would contribute. In a harmonic oscillator basis, the nonvanishing transition amplitude of $\psi(3770) \rightarrow \gamma\eta_c(\eta_c(2S))$ is the same order as that of $\psi(3686) \rightarrow \gamma\eta_c(\eta_c(2S))$. Since a quantitative estimate of the quark model constructions, Ref. [8] only concentrates the IML mechanism that present the unquenched contributions. The IML transitions predict $\Gamma(\psi(3770) \rightarrow \gamma\eta_c) = (17.14^{+22.93})$ keV and $\Gamma(\psi(3770) \rightarrow \gamma\eta_c(2S)) = (1.82^{+1.95})$ keV, which are in a reasonable order of magnitude, although uncertainties appear to be significant. Interestingly, the IML contributions are the same order as the LQCD results [9]. This implies

that interferences between the quenched and unquenched amplitudes could be important for the $\psi(3770)$ radiative decays. As a consequence, the radiative transition of $\psi(3770)$ could become either abnormally strong or significantly small in comparison with potential quark model expectations. Experimental measurement of these radiative transitions would be helpful for providing further constraint on the IML contributions.

Recently, totally 2.92 fb^{-1} data has been accumulated at $\sqrt{s} = 3.773 \text{ GeV}$ with the BESIII detector at BEPCII, which is the largest data sample taken at $\sqrt{s} = 3.773 \text{ GeV}$ in the world at present. It offers us great opportunities to observe the radiative transitions between $\psi(3770)$ and $\eta_c(\eta_c(2S))$. Although the known branching fractions of $\eta_c(\eta_c(2S))$ decays are small, tagging of the final states of $\eta_c(\eta_c(2S))$ decay can really help to reduce the backgrounds(BG). And for $\eta_c(2S)$, very few decay modes were already observed in experiments, so the decay modes $\eta_c(\eta_c(2S)) \rightarrow K_S^0 K^\pm \pi^\mp$ are chosen as the first try to search for $\eta_c(\eta_c(2S))$ in $\psi(3770)$ radiative transition at BESIII considering the decay rates of $\eta_c(\eta_c(2S))$ and background level. It is sure that we are searching for a small signal and we do not want to be biased by the fluctuation of data. We also know that at this moment, the full simulation is still in the stage of fine tuning and the difference between data and simulation cannot be neglected. So it is really hard to believe the optimization of the event selection criteria with MC samples. So the event selection and analysis methods will be developed by looking related distributions of MC and data samples. The processes with the same final states $e^+e^- \rightarrow \gamma(\text{ISR}) J/\psi, J/\psi \rightarrow K_S^0 K^\pm \pi^\mp$ will be taken as control sample to validate these selection and to check MC simulations.

2 The BEPCII and BESIII detector

BEPCII/BESIII are a major upgrade of BEPCI/BESII at the BEPC accelerator for the studies of light and charm quarks physics and τ -charm physics with the highest accuracy achieved until now. The designed peak luminosity of the double-ring e^+e^- collider, BEPCII, is $10^{33} \text{ cm}^{-2}\text{s}^{-1}$ at about 3.7 GeV . The BESIII detector with a geometrical acceptance of 93% of 4π , consists of the following main components [10]:

- a drift chamber (MDC) equipped with 6796 signal wires and 21884 field wires arranged in a small cell configuration with 43 layers working in a gas mixture of He(40%) and C_3H_8 (60%). The single wire resolution on average is 135 m and the momentum resolution for charged particles in a 1 T magnetic field is 0.5% at 1 GeV;
- an electromagnetic calorimeter (EMC) made of 6240 CsI(Tl) crystals arranged in a cylindrical shape plus two endcaps. The energy resolution is 2.5% in the barrel and 5% in the endcaps at 1.0 GeV; the position resolution is 6 mm in the barrel and 9 mm in the endcaps at 1.0 GeV; photon energy resolution at BESIII is much better than that at BESII and comparable to those at CLEO and Crystal Ball; the peaking time of the energy deposit in the EMC is recorded with a precision of 50 ns. Such a time stamp can be used to identify the energy deposit in coincidence with the beam-crossing, hence significantly reduce the time uncorrelated background;
- a Time-Of-Flight system (TOF) for particle identification made of 176 pieces, 2.4 m long plastic scintillators arranged as a cylinder with two layers for the barrel, 5 cm thick each, and 96 fan-shaped, 5 cm thick, plastic scintillators for two endcaps; time resolution is about 80 ps in the barrel, and about 110 ps in the endcaps, corresponding to a K/π separation of more than 2σ level up to about 1.0 GeV;

- a muon chamber system (MUC) made of 1000 m² of Resistive Plate Chambers (RPC) arranged in 9 layers in the barrel and 8 layers in the endcaps. The position resolution is about 2 cm.

3 Data sets and MC simulation

3.1 Data sets

The results reported in this analysis memo are based on the data taken at $\sqrt{s} = 3.773$ GeV during the time period from December 2010 to May 2011. The total integrated luminosity ($\int \mathcal{L} dt$) collected was approximately 2.92 fb⁻¹.

3.2 Software framework and MC simulation

The software framework used for the data analysis is BESIII Offline Software System (BOSS) [11], which is developed from Gaudi [12]. This analysis is performed under BOSS version 6.6.2.

Monte-Carlo (MC) simulation of the full detector is used to determine the detection efficiency of each channel, optimize event selection criteria and estimate backgrounds. The GEANT4-based simulation software, BOOST (BESIII Object Oriented Simulation) [13], provides an event generator, contains the detector geometry description, and simulates the detector response and signal digitization. For each signal mode analyzed in this memo, an exclusive MC sample is generated to study the reconstruction efficiency. Meanwhile, for some dominant background modes, exclusive MC samples are also generated to understand the background shapes. The decay model used for $\psi(3770) \rightarrow \gamma\eta_c(\eta_c(2S))$ is JPE. The decay model for $\psi(3770) \rightarrow \gamma\chi_{c1}$ is P2GC1. The decay mode for $e^+e^- \rightarrow \gamma_{ISR}J/\psi$ is VECTORISR. The charmonium decays ($X \rightarrow K_S^0 K^\pm \pi^\mp$) are generated according to MassH2 (see Section 8.8 for more information). Where K_S^0 is required to decay fully into $\pi^+\pi^-$ and π^0 is required to decay into $\gamma\gamma$. All the exclusive MC samples are listed in Table 1. To investigate possible background contaminations, a few inclusive MC samples for different processes are also generated. These are $e^+e^- \rightarrow \psi(3770) \rightarrow D^0\bar{D}^0$, $e^+e^- \rightarrow \psi(3770) \rightarrow D^+D^-$, $e^+e^- \rightarrow \psi(3770) \rightarrow \text{non-}D\bar{D}$, $e^+e^- \rightarrow \gamma_{ISR}\psi(3686)$, $e^+e^- \rightarrow \gamma_{ISR}J/\psi$, $e^+e^- \rightarrow q\bar{q}$ and $e^+e^- \rightarrow \tau^+\tau^-$. The event number and luminosity for each inclusive MC sample are listed in Table 2. All these MC samples are reconstructed with BOSS 6.6.2.

Table 1: Number of generated exclusive MC samples

Decay modes	Number of events
$\psi(3770) \rightarrow \gamma\eta_c, \eta_c \rightarrow K_S^0 K^+ \pi^- + \text{c.c.}$	100000
$\psi(3770) \rightarrow \gamma\eta_c(2S), \eta_c(2S) \rightarrow K_S^0 K^+ \pi^- + \text{c.c.}$	100000
$\psi(3770) \rightarrow \gamma\chi_{c1}, \chi_{c1} \rightarrow K_S^0 K^+ \pi^- + \text{c.c.}$	100000
$e^+e^- \rightarrow \gamma_{ISR}J/\psi, J/\psi \rightarrow K_S^0 K^+ \pi^- + \text{c.c.}$	100000
$e^+e^- \rightarrow \gamma_{ISR}J/\psi, J/\psi \rightarrow K\bar{K}^*(892) + \text{c.c.} \rightarrow K_S^0 K^\pm \pi^\mp$	100000
$e^+e^- \rightarrow \pi^0 K_S^0 K^+ \pi^- + \text{c.c.}$	1000000
$e^+e^- \rightarrow K_S^0 K^\pm \pi^\mp (\gamma_{ISR}/\gamma_{FSR})$	4000000

Table 2: Number of events and luminosity of inclusive MC samples

Physics	Number of events	Luminosity scale
$e^+e^- \rightarrow \psi(3770) \rightarrow D^0\bar{D}^0$	111M	10 \times
$e^+e^- \rightarrow \psi(3770) \rightarrow D^+D^-$	87M	10 \times
$e^+e^- \rightarrow \psi(3770) \rightarrow \text{non-}D\bar{D}$	15M	10 \times
$e^+e^- \rightarrow \gamma_{ISR}\psi(3686)$	51M	5 \times
$e^+e^- \rightarrow \gamma_{ISR}J/\psi$	16.5M	5 \times
$e^+e^- \rightarrow q\bar{q}$	183M	5 \times
$e^+e^- \rightarrow \tau^+\tau^-$	45M	5 \times

4 General event selection

In the selection of events with the final states $\gamma K_S^0 K^\pm \pi^\mp$, $K_S^0 \rightarrow \pi^+ \pi^-$ is used to tag K_S^0 . So firstly, the candidates are required to have more than 4 charged tracks in total and at least 1 good photon.

4.1 Good photon selection

For photon selection, the following cuts are used to identify good photons from the neutral showers reconstructed by Electro-Magnetic Calorimeter (EMC):

- TDC window: $0 \leq t \leq 14$, here t (in unit of 50 ns) is the time information of EMC. The EMC timing of the photon candidates must be coincident with collision events to suppress electronics noise and energy deposits unrelated to the event.
- Energy threshold: $E_\gamma > 25$ MeV for the barrel of EMC ($|\cos\theta| < 0.80$), $E_\gamma > 50$ MeV for the endcap of EMC ($0.86 < |\cos\theta| < 0.92$).
- The opening angle between a candidate shower and the closest charged track should be larger than 20° . It was calculated by the angle between the position of the center crystal of the shower and the extrapolated position on EMC of the charged tracks.

4.2 K_S^0 selection

K_S^0 is identified via the decay $K_S^0 \rightarrow \pi^+ \pi^-$. The following selection criteria is used for K_S^0 .

- Since K_S^0 has a relatively long lifetime, it will travel a detectable distance to the point where it decays into daughter particles. So the daughter tracks of K_S^0 , π^\pm , do not originate from the interaction point (IP). We imposed no constraints on R_{xy} or R_z of these types of tracks.
- To reconstruct K_S^0 , common vertex fit is performed for each oppositely charged track pair in every event, where all the charged tracks are assumed to be pions. In order to

reconstruct the decay point of K_S^0 , we performed secondary vertex fit on the opposite charged pion pair. That is the mother particles reconstructed from the previous fits are fitted to point to the run-dependent IP. The IP is determined by averaging the event vertexes in each run. No extra χ^2 cut is required for the secondary vertex fit.

- To suppress the random combinatorial backgrounds and reject the mis-combinations of pion pair, the decay length of K_S^0 is required to be larger than twice the calculated resolution, i.e. $L/\sigma_L > 2$, where L represents the flight distance of K_S^0 and σ_L is the error of the flight distance. No extra χ^2 cut is imposed on the decay length fit. Figure 2(a) shows the distribution of decay length of K_S^0 candidates for both signal MC and data, while Fig. 2(b) illustrates the distributions of L/σ_L .
- The secondary vertex constrained tracks must have an invariant mass within 10 MeV/ c^2 around the K_S^0 nominal mass, $|m_{\pi^+\pi^-} - m_{K_S^0}| < 10$ MeV/ c^2 , which is about 3σ deviation to the nominal mass. The invariant mass distributions of charged pion pair are shown in Fig. 2(c). If there are more than one K_S^0 reconstructed, the one whose mass is closest to K_S^0 nominal mass is kept as the candidate.

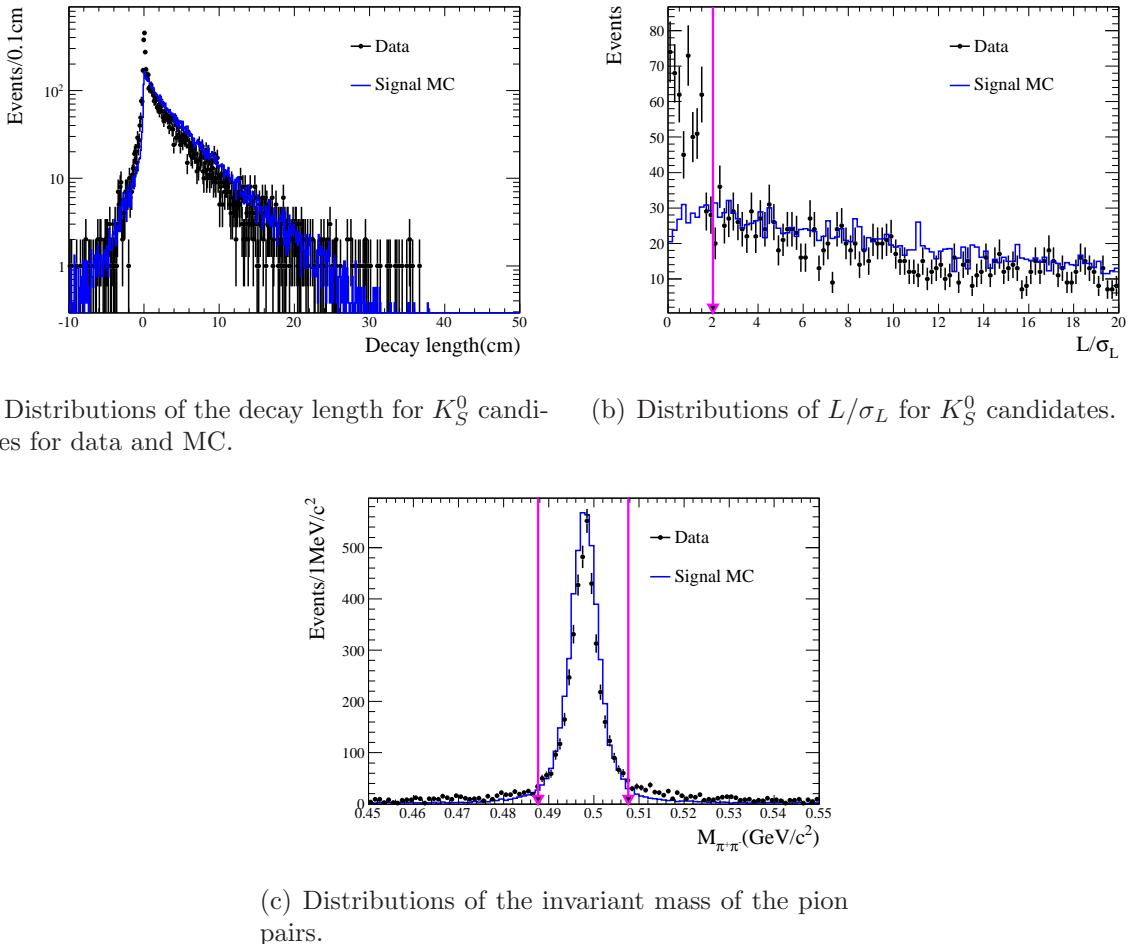


Figure 2: Comparison between signal MC and data on the distributions used in the K_S^0 reconstruction.

4.3 Good charged track selection

Except the two charged tracks from K_S^0 decay, other charged tracks are required to satisfy the following criteria:

- $R_{xy} < 1.0$ cm and $R_z < 10.0$ cm, where R_{xy} and R_z refer to the closest approach distance from the run-by-run-determined interaction (IP) point to the reconstructed track in x - y plane and z direction (along the beam direction), respectively.
- Polar angle of each track in MDC: $|\cos \theta| < 0.93$, where θ is the angle between the direction of tracks at IP and the beam direction (z axis).
- Only 2 good charged tracks with zero net charge are required to pass the above selection criteria in MDC.

4.4 Kinematic fit

A general four-constraint (4C) kinematic fit is performed to select the transition photon by minimizing χ^2 , which can reject background and improve the resolution of signals. The total four-momenta of the reconstructed hadronic decay and radiative photon candidate is constrained to the initial $\psi(3770)$ four-momentum, while the track information at the secondary vertex is taken as input in the kinematic fit.

4.5 Particle identification

Except for the tracks selected as daughters of K_S^0 , the charged kaons and pions are identified by means of dE/dx and TOF measurements. The combined probabilities of PID ($\text{prob}(K)$ or $\text{prob}(\pi)$) for kaon or pion hypothesis were calculated. In order to improve selection efficiency, we do not apply PID cut here. The remaining pair of charged tracks in each event can be $K^+\pi^-$ or $K^-\pi^+$. With these two assumptions, four-constraint (4C) kinematic fit and PID are performed. For each assumption, all the good photons are looped and the one with the smallest χ_{4C}^2 is regarded as the transition photon. Furthermore, $\chi_{PID+4C}^2 = \chi_{4C}^2 + \chi_{K^\pm}^2 + \chi_{\pi^\mp}^2$ is used to identify the final state particles, where χ_{4C}^2 is the χ^2 of 4C kinematic fit and $\chi_{K^\pm}^2$, $\chi_{\pi^\mp}^2$ are the χ^2 of K , π PID. Figure 3 shows the scatter plots of χ_{PID+4C}^2 with different assumptions, from which we can see that the χ_{PID+4C}^2 peaks at small values with the right assumption. So the particle types of the other track pair are determined by choosing the smaller χ_{PID+4C}^2 .

5 Background suppression

5.1 4C kinematic fit

In order to give further rejection of the backgrounds having similar final states like $\pi^0(\gamma\gamma)K_S^0K^\pm\pi^\mp$, $K_S^0K^\pm\pi^\mp$, $\gamma\pi^+\pi^-K^+K^-$ and so on, the 4C kinematic fits are required to be reasonably good. The χ_{4C}^2 cut is optimized using the figure of merit (FOM) $\frac{S}{\sqrt{S+B}}$, where S in the numerator stands for the signals which come from η_c signal MC simulation and $S+B$ in the denominator stands for data. Figure 4(a) shows the distribution of FOM versus χ_{4C}^2 , and the distribution of efficiency versus χ_{4C}^2 is shown in Fig. 4(b). The comparison between data and MC on the distribution of χ_{4C}^2 in η_c mass region are shown in Fig. 5. According to these distributions, the selection $\chi_{4C}^2 < 20$ is adopted for all the interesting decay modes.

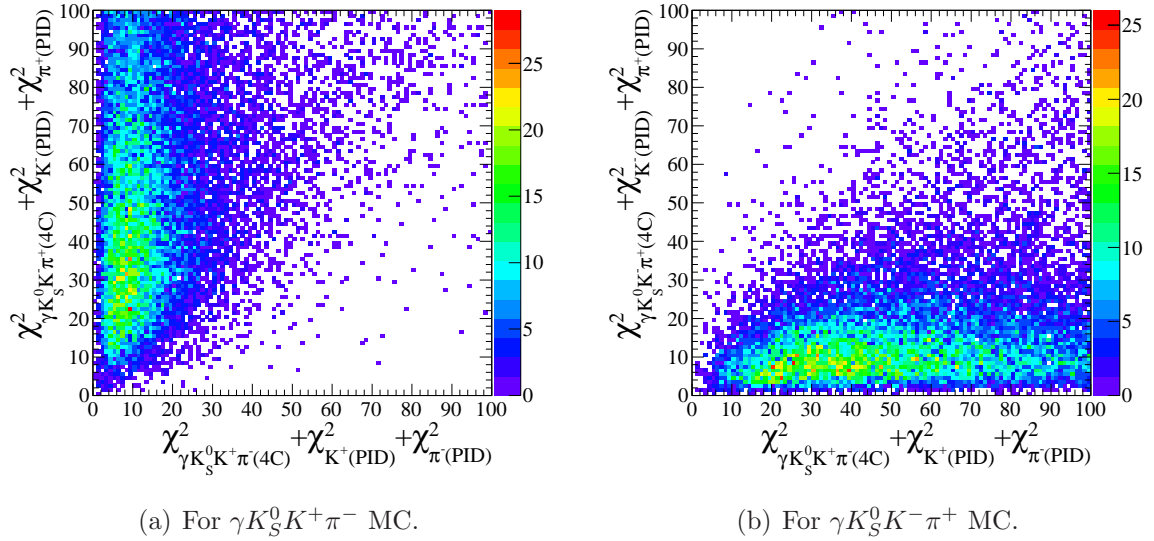


Figure 3: Scatter plots of χ^2_{PID+4C} with different assumptions.

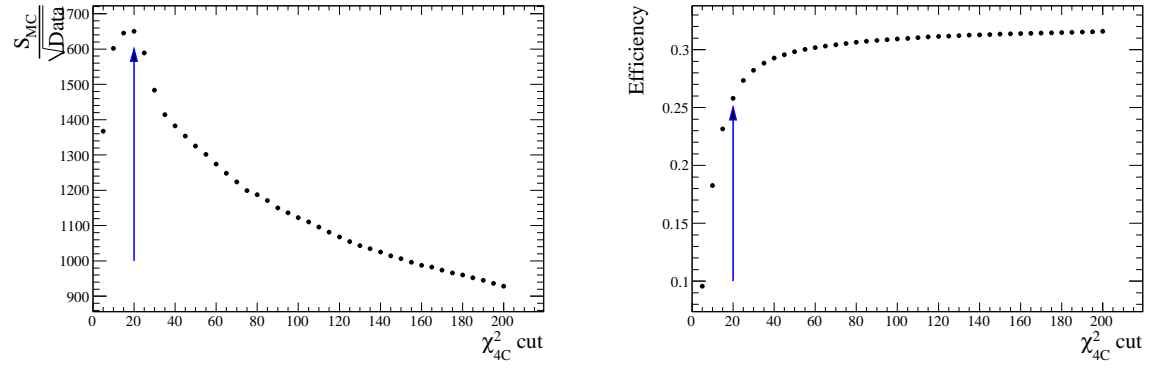


Figure 4: Optimization results of χ^2_{4C} cut

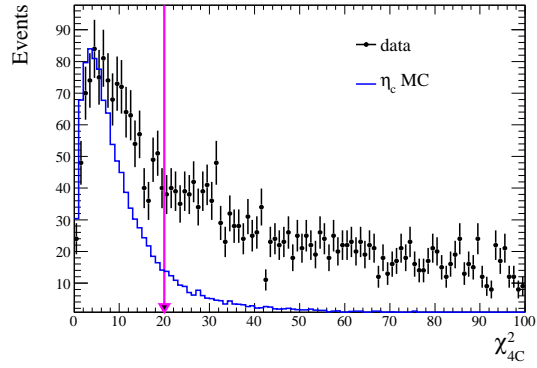
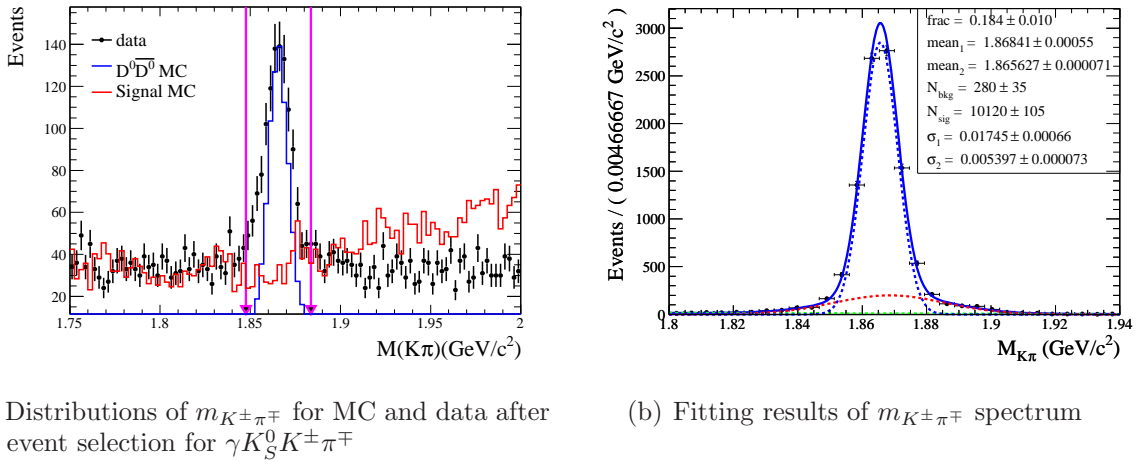


Figure 5: The χ^2_{4C} distributions for η_c MC and data.

5.2 D^0 events rejection (D^0 veto)

As already mentioned, $\psi(3770)$ is a resonance which is above the $D\bar{D}$ threshold that decay predominantly into pairs of open-flavor charmed meson final states. This fraction is so large that even a small probability for these events with similar final states to survive can make a significant contamination. According to the $\psi(3770) \rightarrow D^0\bar{D}^0, D^+D^-$ inclusive MC samples, the leading decay modes for this kind of backgrounds are $\psi(3770) \rightarrow D^0\bar{D}^0, \bar{D}^0 \rightarrow \pi^0 K_S^0, D^0 \rightarrow \pi^+ K^-$ or $\psi(3770) \rightarrow D^0\bar{D}^0, D^0 \rightarrow \pi^0 K_S^0, \bar{D}^0 \rightarrow \pi^- K^+$. There is a clear D^0 signal on the mass spectrum $m_{K^\pm\pi^\mp}$ for both inclusive MC and data, while there is only a small fraction of events around the D^0 mass on $m_{K^\pm\pi^\mp}$ for the signal $\psi(3770) \rightarrow \gamma\eta_c(\eta_c(2S)), \eta_c(\eta_c(2S)) \rightarrow K_S^0 K^\pm\pi^\mp$ as shown in Fig. 6(a). In order to reduce the background, we require $|m_{K^\pm\pi^\mp} - m_{D^0}| > 3\sigma$, where m_{D^0} is the D^0 nominal mass; σ is got from fitting $m_{K^\pm\pi^\mp}$ spectrum of survived $D^0\bar{D}^0$ inclusive MC events as shown in Fig. 6(b). The spectrum is described by a Double-Gaussian plus 1st order Chebychev polynomial. The average σ of $m_{K^\pm\pi^\mp}$ is 5.4 MeV after $\gamma K_S^0 K^\pm\pi^\mp$ preliminary selection. The relative efficiency loss of this selection is about 1.8% for η_c , and 0.5% for $\eta_c(2S)$.



(a) Distributions of $m_{K^\pm\pi^\mp}$ for MC and data after the event selection for $\gamma K_S^0 K^\pm\pi^\mp$

(b) Fitting results of $m_{K^\pm\pi^\mp}$ spectrum

Figure 6: D^0 events rejection.

5.3 π^0 events rejection (π^0 veto)

To suppress the background from the continuum process $e^+e^- \rightarrow \pi^0 K_S^0 K^\pm\pi^\mp$ further after the selection criterion $\chi_{4C}^2(\gamma K_S^0 K^\pm\pi^\mp) < 20$ as mentioned in Section 5.1, we loop in all photon candidates to perform a 4C-kinematic fit and require that the χ_{4C}^2 of the 4C-kinematic fit satisfy: $\chi_{4C}^2(\gamma K_S^0 K^\pm\pi^\mp) < \chi_{4C}^2(\gamma\gamma K_S^0 K^\pm\pi^\mp)$. This cut will deduct only 2.3% efficiency for η_c and 2.5% for $\eta_c(2S)$ while it can remove 20.4% $e^+e^- \rightarrow \pi^0 K_S^0 K^\pm\pi^\mp$ background. Fig. 7 shows the scatter plots of $\chi_{4C}^2(\gamma K_S^0 K^\pm\pi^\mp)$ v.s. $\chi_{4C}^2(\gamma\gamma K_S^0 K^\pm\pi^\mp)$. Fig. 7(a) and Fig. 7(b) are MC simulated $\psi(3770) \rightarrow \gamma\eta_c(\eta_c(2S)), \eta_c(\eta_c(2S)) \rightarrow K_S^0 K^\pm\pi^\mp$. Fig. 7(c) and Fig. 7(d) are MC simulated $e^+e^- \rightarrow \pi^0 K_S^0 K^\pm\pi^\mp$ and $e^+e^- \rightarrow q\bar{q}$ inclusive MC events, respectively.

5.4 Cut flow and reconstruction efficiency

All the selection criteria are introduced in the above sections. In this analysis, we will apply the same selection criteria for $\psi(3770) \rightarrow \gamma\eta_c, \eta_c \rightarrow K_S^0 K^\pm\pi^\mp$ and $\psi(3770) \rightarrow \gamma\eta_c(2S), \eta_c(2S) \rightarrow K_S^0 K^\pm\pi^\mp$. The efficiencies for each selection step in $\psi(3770) \rightarrow \gamma\eta_c, \eta_c \rightarrow K_S^0 K^\pm\pi^\mp, \psi(3770) \rightarrow$

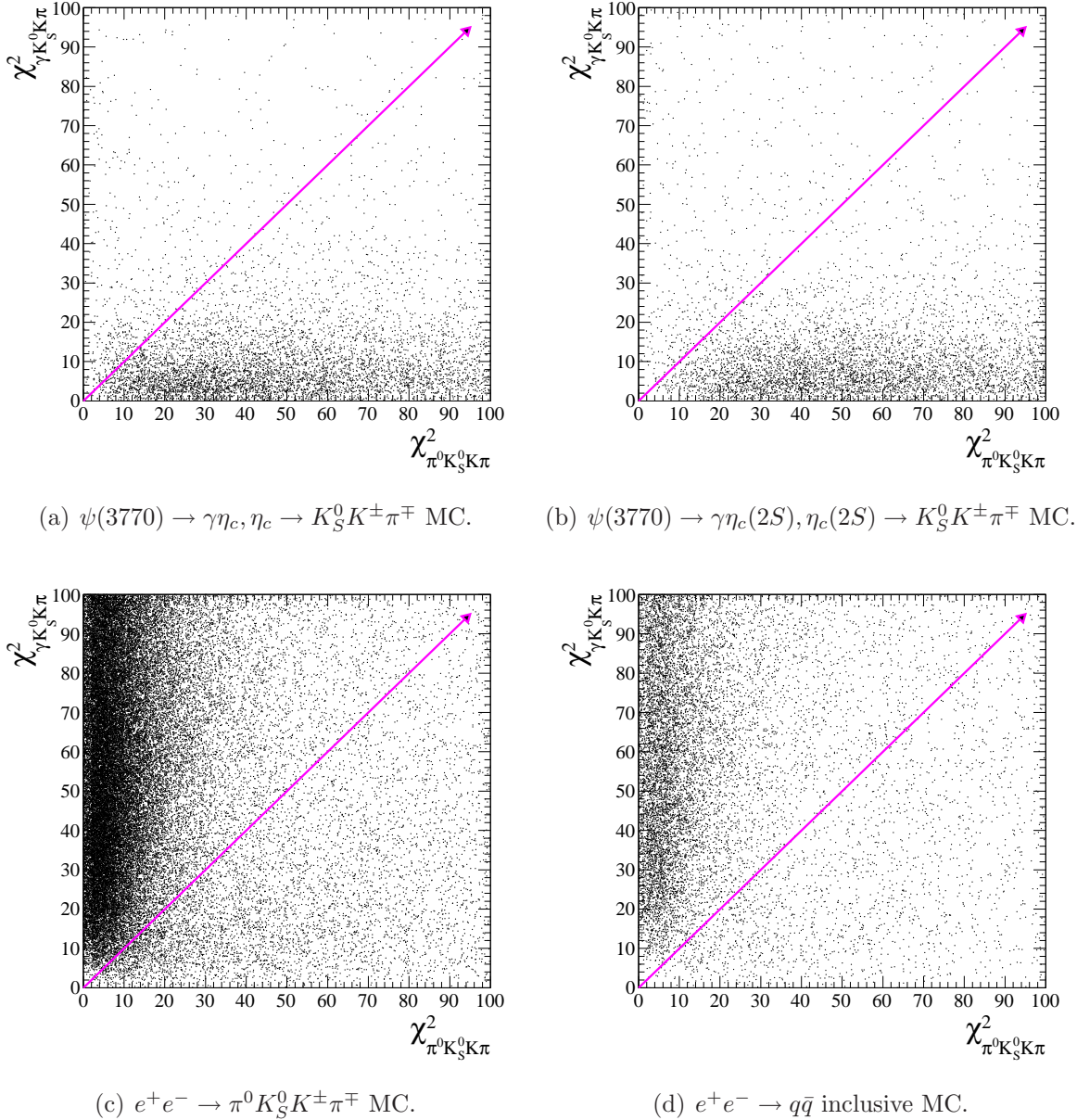


Figure 7: Scatter plots of $\chi^2_{4C}(\gamma K_S^0 K^\pm \pi^\mp)$ v.s. $\chi^2_{4C}(\gamma\gamma K_S^0 K^\pm \pi^\mp)$.

$\gamma\eta_c(2S), \eta_c(2S) \rightarrow K_S^0 K^\pm \pi^\mp$ and also $e^+e^- \rightarrow \gamma_{ISR} J/\psi, J/\psi \rightarrow K_S^0 K^\pm \pi^\mp, \psi(3770) \rightarrow \gamma\chi_{c1}, \chi_{c1} \rightarrow K_S^0 K^\pm \pi^\mp$ for reference are shown in Table 3. The reconstruction efficiencies are 27.69%, 25.21%, 5.89%, and 28.70%, respectively.

Table 3: Cut flows of different signal channels.

Selection	$\psi'' \rightarrow \gamma\eta_c$		$e^+e^- \rightarrow \gamma_{ISR} J/\psi$		$\psi'' \rightarrow \gamma\eta_c(2S)$		$\psi'' \rightarrow \gamma\chi_{c1}$	
	Number	Efficiency	Number	Efficiency	Number	Efficiency	Number	Efficiency
Total Number	100000	100%	100000	100%	100000	100%	100000	100%
$N_{trk} \geq 4$	73266	73.3%	73856	73.9%	75640	75.6%	76236	76.2%
$1 \leq N_\gamma \leq 10$	65421	89.3%	36995	50.1%	65191	86.2%	68884	90.4%
K_S^0 candidates	63075	96.4%	35844	96.9%	62920	96.5%	66750	96.9%
$N_{goodtrk} = 2, \Sigma Q_i = 0$	54079	85.7%	30281	84.5%	55246	87.8%	58000	86.9%
$M(K_S^0)$ Mass Window	45290	83.7%	25269	83.4%	44551	80.6%	46932	80.9%
K_S^0 decay length cut	42262	93.3%	23833	94.3%	42113	94.5%	44427	94.7%
Pass 4C	35868	84.9%	7529	31.6%	34440	81.8%	37376	84.1%
Veto D^0	35294	98.4%	7391	98.2%	34272	99.5%	36977	98.9%
Veto π^0	34477	97.7%	7270	98.4%	33439	97.6%	36063	97.5%
$\chi_{4C}^2 < 20$	28133	81.6%	5890	81.0%	25566	76.5%	28511	79.1%
Fitting range	27866	99.1%	5890	100%	25240	98.7%	28464	99.8%
Reconstruction efficiency	27.87%		5.89%		25.24%		28.46%	

5.5 MC and data comparison

The performance of the MC simulation is checked by comparing several physical variables of data and MC events with all cuts applied. All the plots shown in Fig. 8 are taken from the reference channel $e^+e^- \rightarrow \gamma_{ISR} J/\psi, J/\psi \rightarrow K_S^0 K^\pm \pi^\mp$ by asking invariant mass $m_{K_S^0 K\pi}^{4C}$ between 3.08 GeV and 3.12 GeV. As shown in Fig. 8, the red dots stand for data, and the solid lines stand for J/ψ MC. The difference between MC and data is not significant.

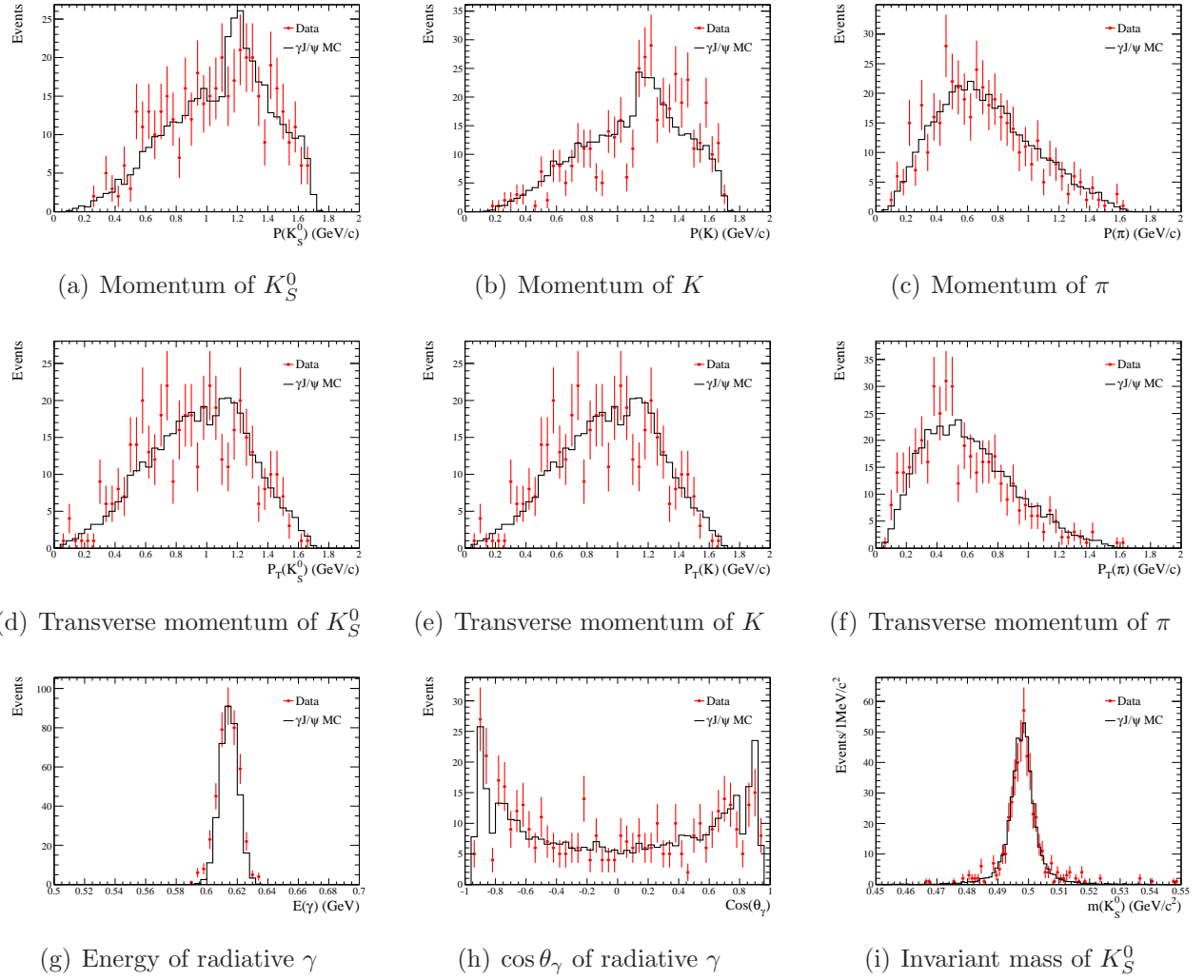


Figure 8: Comparison of physical variables between data and MC.

6 Measurement of $\psi(3770) \rightarrow \gamma\eta_c, \eta_c \rightarrow K_S^0 K^\pm \pi^\mp$

6.1 Background study

6.1.1 Backgrounds estimated by the inclusive MC samples

In this analysis, only the backgrounds with $m_{K_S^0 K\pi}$ around η_c mass are crucial. But the processes $e^+e^- \rightarrow \gamma(\text{ISR}) J/\psi, J/\psi \rightarrow K_S^0 K^\pm \pi^\mp$ contribute exactly the same final states and it gives a big peak just above η_c mass on the $m_{K_S^0 K\pi}$ distribution. As already mentioned, this clear signal from ISR process will be taken as the reference channels. So the backgrounds in a larger mass range $2.7 \text{ GeV}/c^2 < m_{K_S^0 K\pi} < 3.2 \text{ GeV}/c^2$ will be investigated. For convenience, the mass range $2.9 \text{ GeV}/c^2 < m_{K_S^0 K\pi} < 3.05 \text{ GeV}/c^2$ will be called η_c mass region (i.e. signal mass region) and the mass region $3.08 \text{ GeV}/c^2 < m_{K_S^0 K\pi} < 3.12 \text{ GeV}/c^2$ will be called J/ψ mass region.

With all the event selection requirements, the mass spectrum of the remaining backgrounds estimated by various inclusive MC sample described in Section 3.2 is shown in Fig. 9. The red dots stand for data, and the histograms filled with colors stand for all kinds of inclusive MC samples. According to the inclusive MC samples, the background is a smooth distribution and there is no enhancement under η_c signal region. The dominant background comes from $e^+e^- \rightarrow q\bar{q}$ events with final states $\pi^0 K_S^0 K^\pm \pi^\mp$. The careful studies on backgrounds are discussed in the following sections.

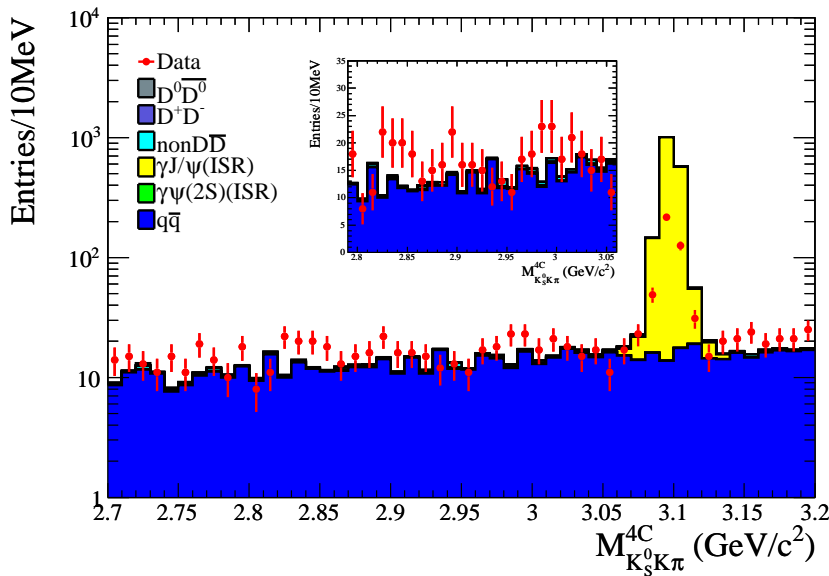


Figure 9: The mass spectrum for the backgrounds predicted by summing inclusive MC samples.

6.1.2 Background from $\pi^0 K_S^0 K^\pm \pi^\mp$

With all these event selection criteria applied, the events from $\pi^0 K_S^0 K^\pm \pi^\mp$ can still contaminate the $\gamma K_S^0 K^\pm \pi^\mp$ candidates if one of the two photons from π^0 decay is soft. In this case, π^0 veto cannot be an efficient way to suppress the remaining $\pi^0 K_S^0 K^\pm \pi^\mp$ background, because only a small fraction of these π^0 with one soft photon can be reconstructed well.

But the mass spectrum for $\pi^0 K_S^0 K^\pm \pi^\mp$ background can be estimated by measuring $\pi^0 K_S^0 K^\pm \pi^\mp$ in data and scaling the measured mass spectrum to the $\gamma K_S^0 K^\pm \pi^\mp$ assumption according to the MC simulation. With a similar event selection procedure:

- The event should contain one and only one good K_S^0 candidate;
- Other charged tracks (except for the π^+, π^- from K_S^0 decays) should pass vertex cut and the number of them must be equal to two with net charge zero;
- 2 or 3 good photons;
- The 4C kinematic fit are performed on the hypothesis $\gamma\gamma K_S^0 K^\pm \pi^\mp$ by looping all the photon pair of π^0 candidates and require $\chi_{4C}^2(\gamma\gamma K_S^0 K^\pm \pi^\mp) < 20$;
- The final state $\pi^0 K_S^0 K^+ \pi^-$ or $\pi^0 K_S^0 K^- \pi^+$ is determined by the smaller $\chi_{PID+4C}^2 = \chi_{4C}^2 + \chi_{K^\pm}^2 + \chi_{\pi^\mp}^2$
- For π^0 candidates, the invariant mass of the two photons selected by 4C kinematic fit should be in the mass window $0.12 \text{ GeV}/c^2 < m_{\gamma\gamma}^{4C} < 0.15 \text{ GeV}/c^2$.

After the above selections we get a $\pi^0 K_S^0 K^\pm \pi^\mp$ data sample. Fig. 10 illustrates the invariant mass of reconstructed π^0 after 4C kinematic fit. The mass of $K_S^0 K^\pm \pi^\mp$ for selected $\pi^0 K_S^0 K^\pm \pi^\mp$ events is still calculated in the same way as $\gamma K_S^0 K^\pm \pi^\mp$ selection, which is shown in Fig. 11(a). According to the simulation with large statistics for $e^+e^- \rightarrow \pi^0 K_S^0 K^\pm \pi^\mp$ MC sample, the $M_{K_S^0 K\pi}^{4C}$ distribution for events passing through the $\pi^0 K_S^0 K^\pm \pi^\mp$ selection (the upper histogram) and the $M_{K_S^0 K\pi}^{4C}$ distribution for those passing through the $\gamma K_S^0 K^\pm \pi^\mp$ selection (the lower histogram) are obtained as shown in Fig. 11(b) and the efficiency ratio of the two event selections f_{scale} (the selections for $\gamma K_S^0 K^\pm \pi^\mp$ and $\pi^0 K_S^0 K^\pm \pi^\mp$) as a function of $M_{K_S^0 K\pi}^{4C}$ is shown in Fig. 11(c), which is defined as:

$$f_{scale} = \frac{\epsilon_{\gamma K_S^0 K\pi}}{\epsilon_{\pi^0 K_S^0 K\pi}} \quad (2)$$

where $\epsilon_{\gamma K_S^0 K\pi}$ is the efficiency of $e^+e^- \rightarrow \pi^0 K_S^0 K^\pm \pi^\mp$ MC sample passing the $\gamma K_S^0 K^\pm \pi^\mp$ selection and $\epsilon_{\pi^0 K_S^0 K\pi}$ is the efficiency of the same sample passing the $\pi^0 K_S^0 K^\pm \pi^\mp$ selection. Finally, the contaminated mass spectrum comes from $\pi^0 K_S^0 K^\pm \pi^\mp$ background is estimated by scaling the measured mass spectrum with the efficiency ratio. As shown in Fig.11(d), the background from $\pi^0 K_S^0 K^\pm \pi^\mp$ distributes smoothly over the mass spectrum without special structure.

6.1.3 Background from $K_S^0 K^\pm \pi^\mp (\gamma_{ISR}/\gamma_{FSR})$

As a consequence of large cross sections for the background processes in continuum $q\bar{q}$ production at the center-of-mass energy of 3.773 GeV, continuum hadronic events make up the dominant background as previously mentioned. Apart from $e^+e^- \rightarrow \pi^0 K_S^0 K^\pm \pi^\mp$, the process $e^+e^- \rightarrow \gamma K_S^0 K^\pm \pi^\mp$ can also contaminate the signal events by initial-state radiated photons, real soft photons from FSR and picked up fake photons. The initial-state radiated photon allows to cover the hadronic final states in the energy range from thresholds up to ≈ 3.773 GeV, so this kind of process should result in a wide $K_S^0 K^\pm \pi^\mp$ invariant mass distribution.

These background events have the same final states as our signal mode which cannot be separated by event selection criteria. An exclusive MC sample for the process $e^+e^- \rightarrow$

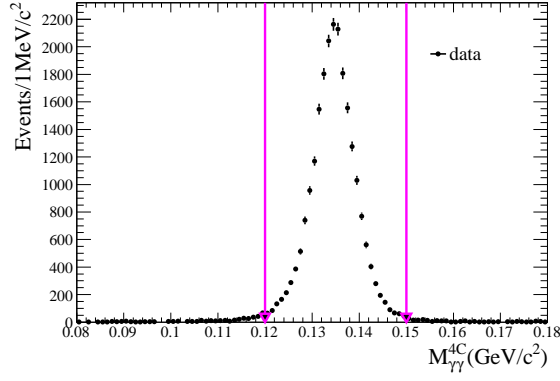
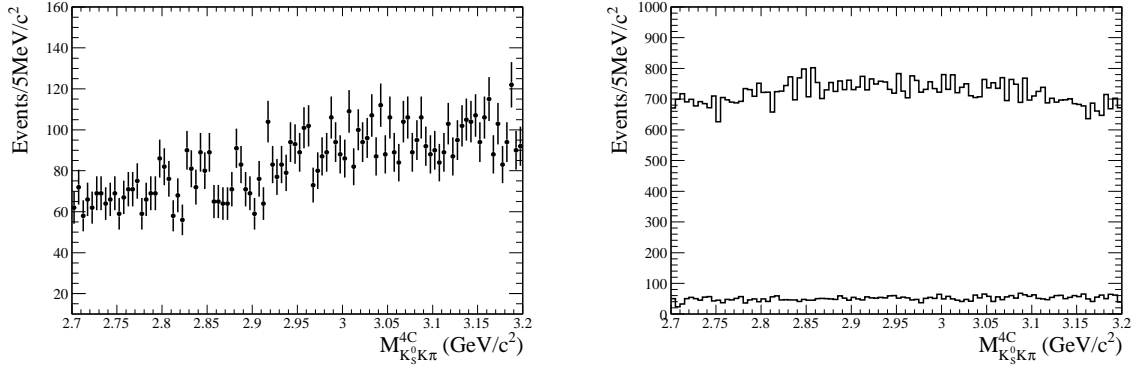
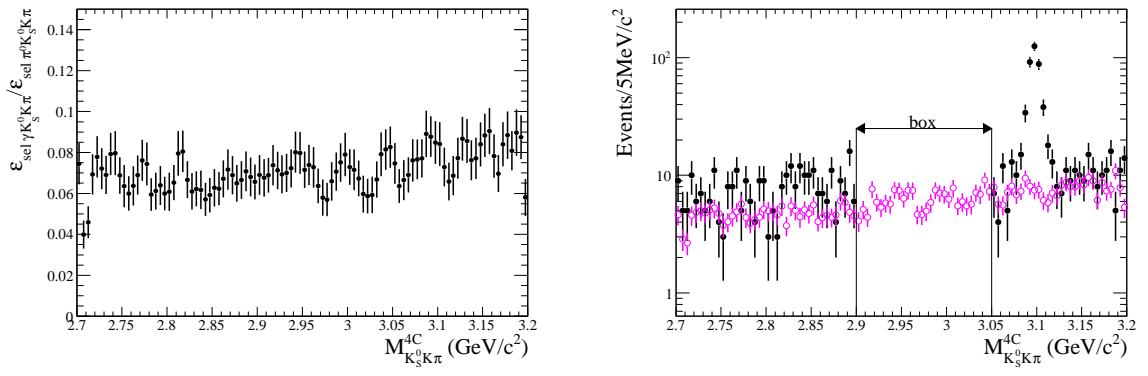


Figure 10: Invariant mass of the two photons for $\pi^0 K_S^0 K^\pm \pi^\mp$ candidates from data.



(a) The $M_{K_S^0 K\pi}$ invariant mass for selected $\pi^0 K_S^0 K\pi$ events from data.

(b) The $M_{K_S^0 K\pi}$ distributions for simulated $\pi^0 K_S^0 K\pi$ MC events pass through the $\pi^0 K_S^0 K\pi$ selection (upper) and those pass through the $\gamma K_S^0 K\pi$ selection (lower).



(c) The ratio of the two histograms in (b).

(d) Pink circles represent the estimated $\pi^0 K_S^0 K\pi$ contribution.

Figure 11: Estimate the $\pi^0 K_S^0 K^\pm \pi^\mp$ background in η_c mass region.

$(\gamma)K_S^0 K^\pm \pi^\mp$ has been generated by ConExc [14] to estimate the contribution of this background. The event generator ConExc is constructed by taking into consideration of the initial state radiation (ISR) with the leading second order correction. It includes the processes of $e^+e^- \rightarrow \text{hadrons}(X_i)$ and $e^+e^- \rightarrow \gamma + \text{hadrons}$, where the photon γ comes from the ISR effects and also FSR. The experimental Born cross section(σ_0) of $e^+e^- \rightarrow K_S^0 K^\pm \pi^\mp$ obtained by the Babar Collaboration [15] and the cross section for the ISR process($\sigma_{e^+e^- \rightarrow \gamma X_i}$) are used as input in the generator.

The $M_{K_S^0 K\pi}^{4C}$ distribution for the survived $e^+e^- \rightarrow (\gamma)K_S^0 K^\pm \pi^\mp$ MC events is shown in Fig. 12. According to the plot, there is a big bump around $3.75 \text{ GeV}/c^2$ where the events with fake photons dominate, and a smooth tail represented by yellow histogram where the FSR events dominate. In low mass region, the events mainly come from ISR process. Here in η_c mass region, the ISR events contribute most.

The invariant mass spectrum of $K_S^0 K^\pm \pi^\mp$ in η_c mass region and the summed mass spectrum of all the estimated backgrounds are shown in Fig. 13 where the estimated backgrounds can describe data well. It indicates that the estimation of backgrounds is reliable. An additional explanation is necessary here: the component of $e^+e^- \rightarrow (\gamma)K_S^0 K^\pm \pi^\mp$ estimated by MC is normalized to data according to the generated cross section of MC sample.

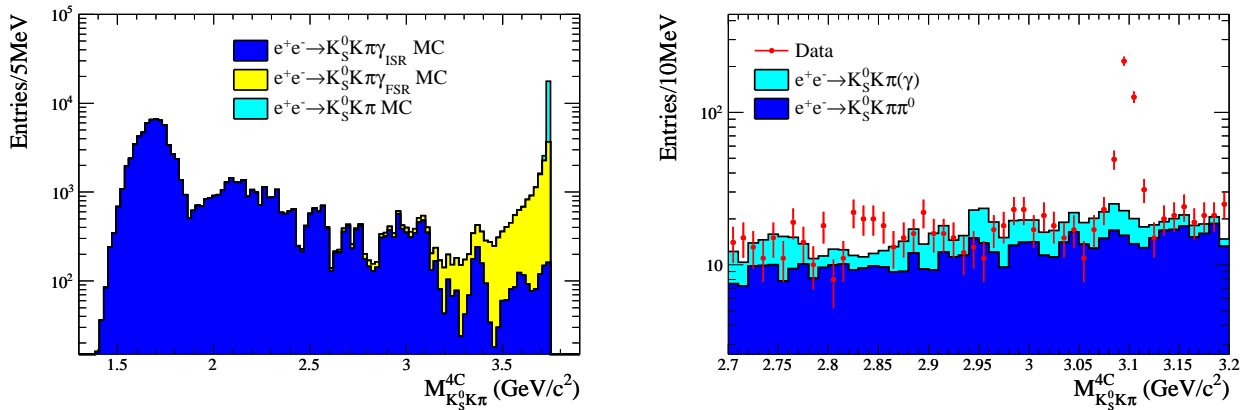


Figure 12: The invariant mass distribution of $K_S^0 K^\pm \pi^\mp$ for $e^+e^- \rightarrow (\gamma)K_S^0 K^\pm \pi^\mp$ MC.

Figure 13: The invariant mass spectrum of $K_S^0 K^\pm \pi^\mp$ in η_c mass region and the summed mass spectrum of all the estimated backgrounds.

6.1.4 Background from $\psi(3686)$ tail

A kind of peaking background source is the tail of the $\psi(3686)$ resonance production at the energy $\sqrt{s} = 3.773 \text{ GeV}$. These background events have the same topology as the decay of $\psi(3770) \rightarrow \gamma \eta_c$ which cannot be separated from $\psi(3770)$ decays by event selection criteria. To get the number of $\psi(3770) \rightarrow \gamma \eta_c$ signal events, the number of the background events of $\psi(3686) \rightarrow \gamma \eta_c$ has to be subtracted from the observed candidate events of $\gamma \eta_c$.

The zeroth-order cross section for $\psi(3686)$ production at the center-of-mass energy of 3.773 GeV is calculated to be 0.025 nb by inserting the $\psi(3686)$ resonance parameters quoted from PDG2012 [16]. The number of the background events $N_{\psi(3686)}^b$ from $\psi(3686)$ decays due to the Breit-weigner tail of $\psi(3686)$ at 3.773 GeV could be estimated by:

$$N_{\psi(3686)}^b = \sigma_{\psi(3686)}^{E_{cm}=3.773 \text{ GeV}} \times \mathcal{L} \times \epsilon_{\psi(3686) \rightarrow \gamma X, X \rightarrow K_S^0 K^\pm \pi^\mp} \times \Pi \mathcal{B}_i \quad (3)$$

where $\sigma_{\psi(3686)}^{E_{cm}=3.773\text{GeV}}$ is zeroth-order cross section for $\psi(3686)$ production at the center-of-mass energy of 3.773 GeV; \mathcal{L} is the integrated luminosity of the data set used in the analysis [17]; $\epsilon_{\psi(3686) \rightarrow \gamma X, X \rightarrow K_S^0 K^\pm \pi^\mp}$ is the detection efficiencies for the final states in question and \mathcal{B}_i denotes the branching fraction for the intermediate resonance decay taken from PDG2012 [16], such as $\mathcal{B}(\psi(3686) \rightarrow \gamma \eta_c)$, $\mathcal{B}(\eta_c \rightarrow K_S^0 K^\pm \pi^\mp)$ and $\mathcal{B}(K_S^0 \rightarrow \pi^+ \pi^-)$. Inserting the corresponding numbers in Eq. 3, we obtain the number of the background events from the $\psi(3686)$ decays at $\sqrt{s} = 3.773$ GeV which will be neglected, as shown in Table 4. The errors arise from the uncertainties in \mathcal{L} , $\sigma_{\psi(3686)}$, ϵ and \mathcal{B}_i .

Table 4: The number of the background events from the $\psi(3686)$ decays at $\sqrt{s} = 3.773$ GeV.

X	$\mathcal{L}[fb^{-1}]$	$\sigma_{\psi'}[nb]$	ϵ	$\mathcal{B}(\psi' \rightarrow \gamma X, X \rightarrow K_S^0 K\pi)$	$\mathcal{B}(K_S^0 \rightarrow \pi^+ \pi^-)[\%]$	$N_{\psi'}^b$
η_c	2.92	0.025	0.285	$(8.16 \pm 1.32) \times 10^{-5}$	69.20 ± 0.05	1.2 ± 0.2

6.1.5 Potential peaking background check

In addition to the above sources of background, we also check whether other processes could contaminate the signal events by analyzing the corresponding inclusive MC samples generated at the center-of-mass energy 3.773 GeV described in Section 3.2. Figure 14 shows the distributions of the invariant mass $M_{K_S^0 K\pi}^{4C}$ for the $D\bar{D}$, non- $D\bar{D}$, ISR J/ψ , ISR $\psi(3686)$, $\tau^+ \tau^-$ and $q\bar{q}$ inclusive MC samples, respectively, which are normalized to the luminosity of real data. We found that there is no obvious peaking background in η_c mass region on each plot.

6.2 Mass spectrum fitting results of real data

6.2.1 The detector resolution

The detector resolution is primarily determined by Dalitz distributed MC simulation for η_c decay mode with zero natural width. The consistency/discrepancy between data and MC is studied by using the decay $e^+ e^- \rightarrow \gamma(\text{ISR}) J/\psi$ with J/ψ decays into the same final states as signal mode. We use a smearing Gaussian function to describe the possible discrepancy between data and MC. As shown in Fig. 15, by fitting the MC-determined $M_{K_S^0 K\pi}^{4C}$ shape convolved by a smearing Gaussian to the data, we determine the Gaussian parameters. The parameters of the smearing Gaussian is determined to be: $\text{mean} = 0.86 \pm 0.40 \text{ MeV}/c^2$, $\sigma = 2.26 \pm 0.93 \text{ MeV}/c^2$. A non-zero mean value of the smearing Gaussian indicates a mass offset.

6.2.2 Fit to the mass spectrum

After applying all the selection criteria discussed above, the invariant mass spectrum $M_{K_S^0 K\pi}^{4C}$ in 2.92 fb^{-1} data is shown in Fig. 17. In order to determine the background better, the mass spectrum range is enlarged ($2.7 \sim 3.2 \text{ GeV}/c^2$) to include J/ψ events.

The line shape for η_c signal should be described carefully before the fitting. The fitting probability density function (P.D.F) for the signal reads:

$$F(m) = \sigma \otimes (\epsilon(m) \times E_\gamma^3 \times BW(m)) \quad (4)$$

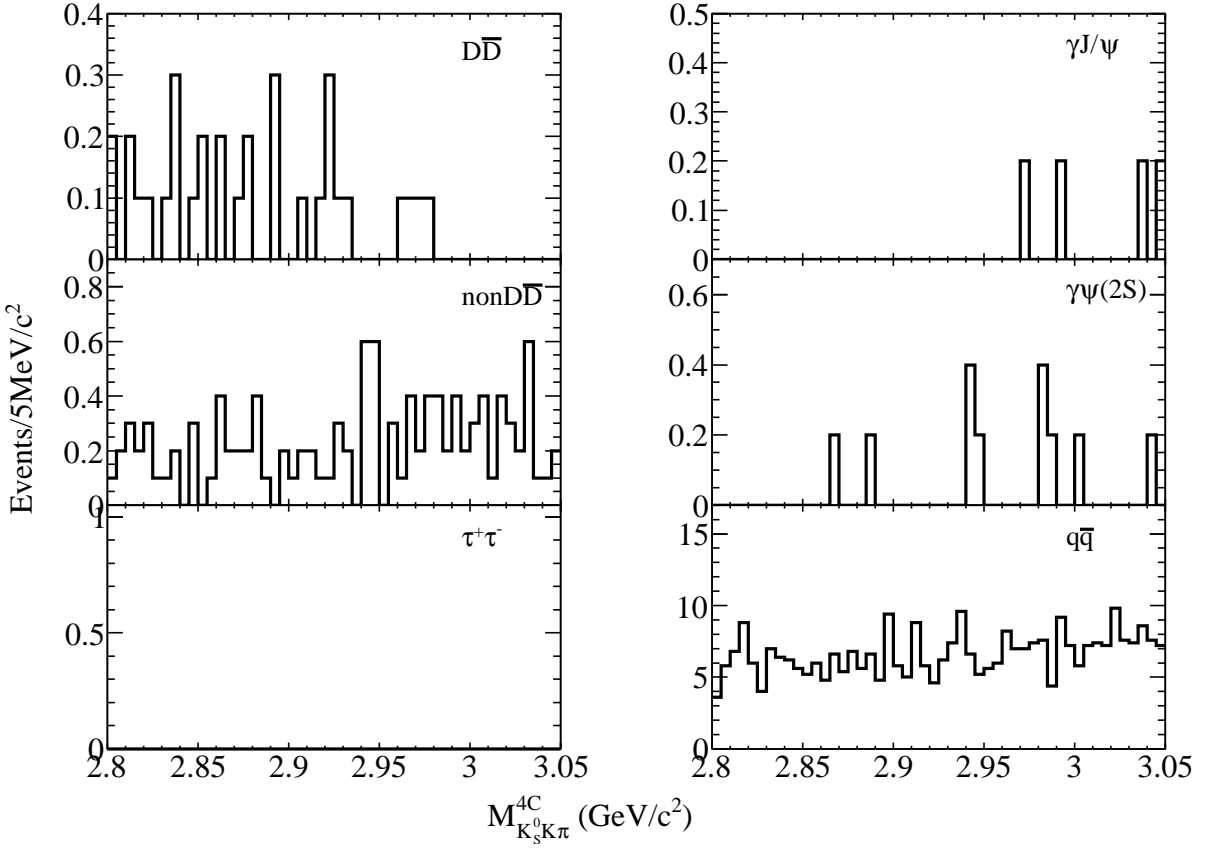


Figure 14: The distributions of $M_{K_S^0 K\pi}^{4C}$ for the surviving background events selected from $D\bar{D}$, ISR J/ψ , non- $D\bar{D}$, ISR $\psi(3686)$, $\tau^+\tau^-$ and $q\bar{q}$ MC samples, respectively.

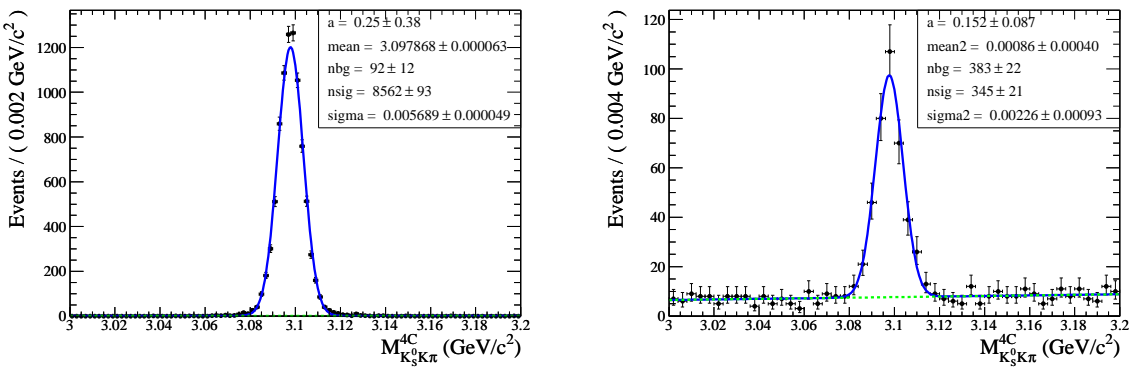


Figure 15: The $M_{K_S^0 K\pi}^{4C}$ distributions for $e^+e^- \rightarrow \gamma(\text{ISR})J/\psi$ with $J/\psi \rightarrow K_S^0 K^\pm \pi^\mp$. Left: for inclusive MC; Right: for data. The data is fitted with the MC-determined shape convolved by a smearing Gaussian with the Gaussian parameters float.

where m is the invariant mass of $K_S^0 K\pi$; σ is the experimental resolution mentioned in Section 6.2.1; $\epsilon(m)$ is mass-dependent efficiency, shown in Fig. 16, which is determined from the MC sample generated according to Dalitz distribution of η_c decay $\eta_c \rightarrow K_S^0 K^\pm \pi^\mp$; $BW(m)$ is the relativistic Breit-Wigner formula, the mass and width of η_c are fixed to the values of PDG2012 [16]; E_γ^3 is radiative transition form factor where $E_\gamma = \frac{m_{\psi(3770)}^2 - m^2}{2m_{\psi(3770)}}$ is the energy of the transition photon in the rest frame of $\psi(3770)$.

The line shape for J/ψ resonance is described by a single Gaussian function with parameters float, while the background is described using a 3rd order Chebychev polynomial with three free parameters. From previous background study, the background in $\psi(3770) \rightarrow \gamma \eta_c$, $\eta_c \rightarrow K_S^0 K^\pm \pi^\mp$ decay mode presents a flat distribution. So it is safe to describe the background by a 3rd order Chebychev polynomial.

An unbinned maximum likelihood fit is performed to the full invariant mass spectrum in Fig. 17. The χ^2/ndf is 0.65. The related results are listed in Table 5. 31.0 ± 18.3 η_c signal events and 349.7 ± 21.0 J/ψ events are extracted from the fit. Since the η_c signal is not so evident that we can also calculate the upper limit of the η_c signal events by using the Bayesian method (fit the invariant mass spectrum with the number of signal set to N_{signal}^i , i from 0 to N_{signal} to get a series of Likelihood values L_i , then the upper limit is determined by finding out the value of N_{signal}^i corresponding to 90% of the numeric integration of the Likelihood distribution). The upper limit of the number of η_c signal events is determined to be 56.8 at 90% C.L. as shown in Fig. 18.

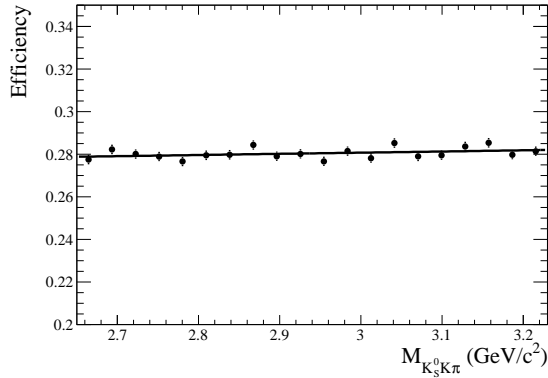


Figure 16: The efficiency as a function of $K_S^0 K^\pm \pi^\mp$ mass for the η_c signal MC generated by MassH2.

Table 5: Results of the fit to the invariant mass spectrum of $K_S^0 K^\pm \pi^\mp$ in η_c mass region. Errors are only statistical.

$\psi(3770) \rightarrow \gamma X$	η_c	U.L. of η_c (90% C.L.)	J/ψ (ISR)	Background
N_{yield}^{data}	31.0 ± 18.3	56.8	349.7 ± 21.0	816.5 ± 36.1

However, we already know that there are 1.2 ± 0.2 peaking background events coming from $\psi(3686)$ decays at the energy $\sqrt{s} = 3.773$ GeV introduced in Section 6.1.4, which are hard to

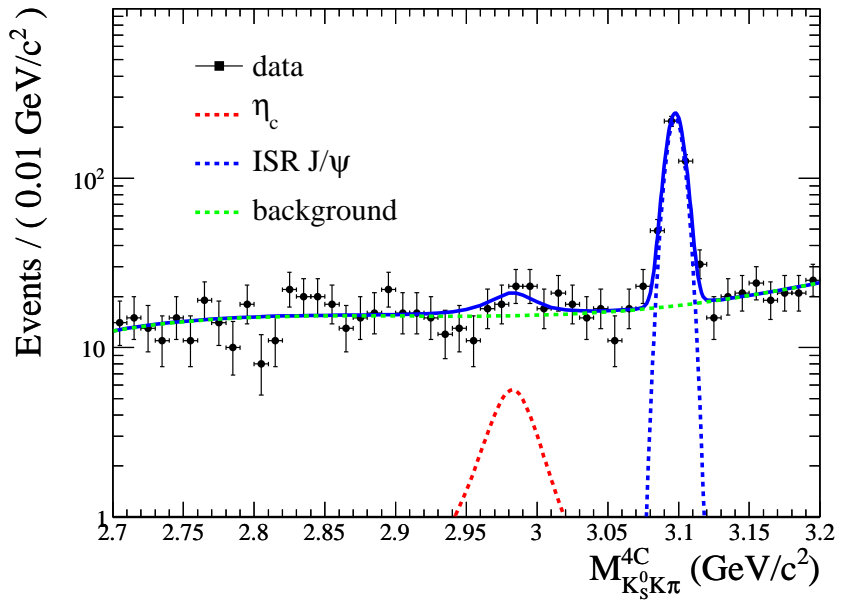


Figure 17: The invariant mass distribution of $K_S^0 K^\pm \pi^\mp$ in η_c mass region for real data. Solid curve shows the result of unbinned maximum likelihood fit.

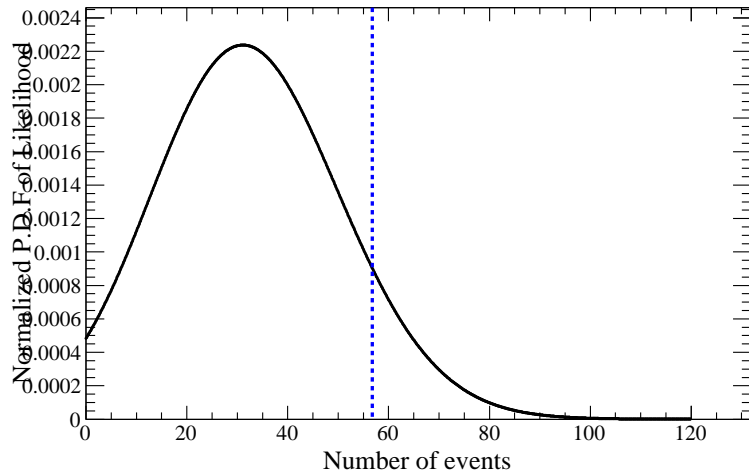


Figure 18: The upper limit of the number of η_c signal events at 90% C.L. from Bayesian approach.

be distinguished from signal events. We use the same line shape to describe signal and this kind of background, then deduct the effect of this background. The deduction of the peaking background is described as below:

- Fitting to the invariant mass spectrum with the number of signal (here signal include the real signal and peaking background $\psi(3686) \rightarrow \gamma\eta_c, \eta_c \rightarrow K_S^0 K^\pm \pi^\mp$) set to N_{signal}^i , i from 0 to N_{signal} to get a series initial likelihood values $L_{initial}^i$.
- The probability distribution (L_{bkg}) of peaking background is a Gaussian distribution.
- Generate random number N_{total}^j according to the distribution of $L_{initial}$, and for each random number, generate N_{bkg}^j according to the distribution of L_{bkg} with requirement $N_{bkg}^j < N_{total}^j$. $N_{signal}^j = N_{total}^j - N_{bkg}^j$ is the probability distribution of signal.

6.2.3 Input/Output check

To check the analysis and fitting method, we have performed a MC Input/Output check. This check is based on the analysis of all kinds of corresponding inclusive MC samples generated at the center-of-mass energy 3.773 GeV and a signal MC sample for $\psi(3770) \rightarrow \gamma\eta_c, \eta_c \rightarrow K_S^0 K^\pm \pi^\mp$ described in Section 3.2. We put these MC samples together with each event weighted. For the inclusive MC samples, the weight factor of each event should be related to the luminosity scale factor of each inclusive MC sample mentioned in Table 2 to make sure that all inclusive MC samples are normalized to data luminosity. The input branching fraction for $\psi(3770) \rightarrow \gamma\eta_c$ is 6.278×10^{-4} according to the theoretical prediction.

By using the same analysis procedure and fitting method as data analysis, we obtain the observed numbers of η_c and J/ψ as shown in Fig. 19. The comparisons of the input and output signal numbers and relative branching fractions are summarized in Table 6. We can see that the output yields are well consistent with the input value within statistic error.

Table 6: The comparisons of the input and output signal numbers and relative branching fractions.

	N_{η_c}	$\mathcal{B}(\psi(3770) \rightarrow \gamma\eta_c)$	$N_{J/\psi}$
Input	59.9	6.278×10^{-4}	1733.4
Output	55.9 ± 17.1	$(5.86 \pm 1.79) \times 10^{-4}$	1703.3 ± 42.3

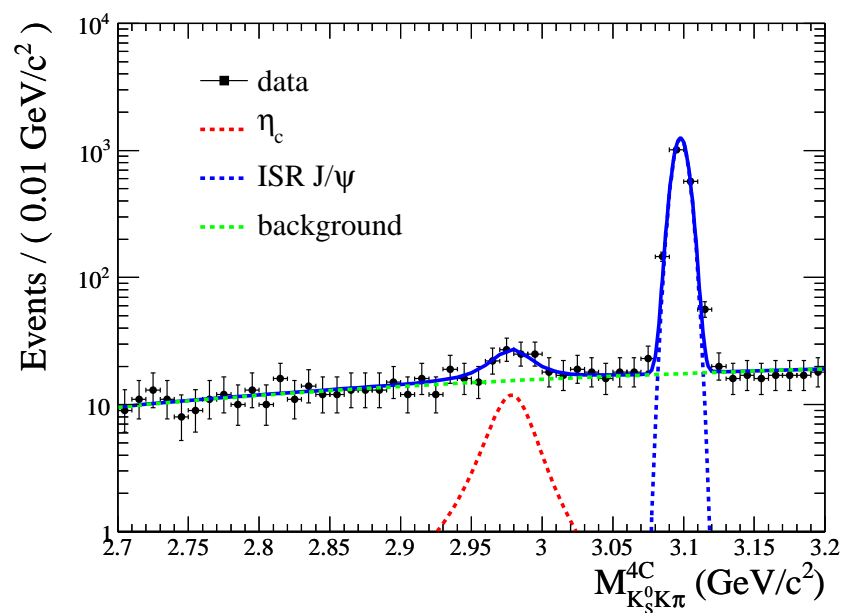


Figure 19: The invariant mass distribution of $K_S^0 K^{\pm} \pi^{\mp}$ in η_c mass region for made up MC samples. Solid curve shows the result of unbinned maximum likelihood fit.

7 Measurement of $\psi(3770) \rightarrow \gamma\eta_c(2S)$, $\eta_c(2S) \rightarrow K_S^0 K^\pm \pi^\mp$

7.1 Background study

7.1.1 Backgrounds estimated by the inclusive MC samples

In this analysis, only the backgrounds with $m_{K_S^0 K\pi}$ around $\eta_c(2S)$ mass are crucial. But the processes $\psi(3770) \rightarrow \gamma\chi_{cJ}$, $\chi_{cJ} \rightarrow K_S^0 K^\pm \pi^\mp (J = 1, 2)$ and $e^+e^- \rightarrow \gamma(\text{ISR})\psi(3686)$, $\psi(3686) \rightarrow K_S^0 K^\pm \pi^\mp$ contribute exactly the same final states and the $m_{K_S^0 K\pi}$ of χ_{c1} and $\psi(3686)$ give two peaks just near $\eta_c(2S)$ mass, however, we didn't find χ_{c2} peak. As already mentioned, these two clear signal from the radiative transition between $\psi(3770)$ and χ_{c1} and ISR process will be taken as the reference channels. So the backgrounds in a larger mass range $3.45 \text{ GeV}/c^2 < m_{K_S^0 K\pi} < 3.71 \text{ GeV}/c^2$ will be investigated. For convenience, the mass range $3.45 \text{ GeV}/c^2 < m_{K_S^0 K\pi} < 3.6 \text{ GeV}/c^2$ will be called χ_{cJ} mass region and the mass range $3.6 \text{ GeV}/c^2 < m_{K_S^0 K\pi} < 3.66 \text{ GeV}/c^2$ will be called $\eta_c(2S)$ mass region (i.e. signal mass region).

With all the event selection requirements, the mass spectrum of the remaining backgrounds estimated by various inclusive MC sample described in Section 3.2 is shown in Fig. 20. The red dots stand for data, and the histograms filled with colors stand for all kinds of inclusive MC samples. According to the inclusive MC samples, the main background in $\eta_c(2S)$ mass region is the continuum process $e^+e^- \rightarrow \gamma^*(\gamma_{\text{ISR}}) \rightarrow K_S^0 K^\pm \pi^\mp(\gamma_{\text{ISR}})$ or $e^+e^- \rightarrow K_S^0 K^\pm \pi^\mp(\gamma_{\text{FSR}})$ (FSR: final state radiation). In χ_{cJ} mass region the main background is $\pi^0 K_S^0 K^\pm \pi^\mp$ which has little effect in $\eta_c(2S)$ mass region due to the phase space distribution of $\pi^0 K_S^0 K^\pm \pi^\mp$. The detailed studies on backgrounds are discussed in the following sections.

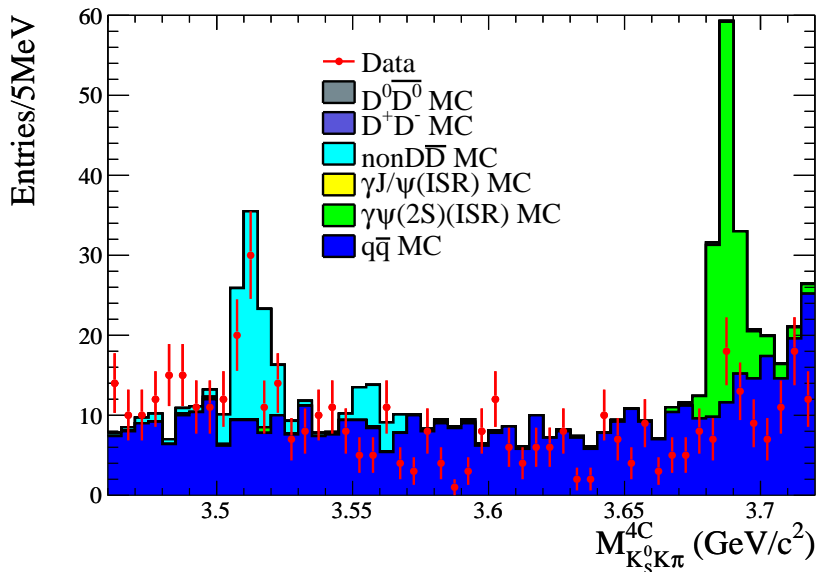


Figure 20: The mass spectrum for the backgrounds predicted by summing inclusive MC samples.

7.1.2 Background from $\pi^0 K_S^0 K^\pm \pi^\mp$

As in the case of the background study for $\psi(3770) \rightarrow \gamma \eta_c$, with all the event selection criteria imposed, the events from $\pi^0 K_S^0 K^\pm \pi^\mp$ can still contaminate the $\gamma K_S^0 K^\pm \pi^\mp$ candidates around the $\eta_c(2S)$ mass region if one of the two photons from π^0 decay is soft. In this case, π^0 veto cannot be an efficient way to suppress the remained $\pi^0 K_S^0 K^\pm \pi^\mp$ background, too. So we use the same method described in Section 6.1.2 to estimate the mass spectrum for $\pi^0 K_S^0 K^\pm \pi^\mp$ background by measuring $\pi^0 K_S^0 K^\pm \pi^\mp$ in data and scaling the measured mass spectrum to the $\gamma K_S^0 K^\pm \pi^\mp$ assumption according to the MC simulation.

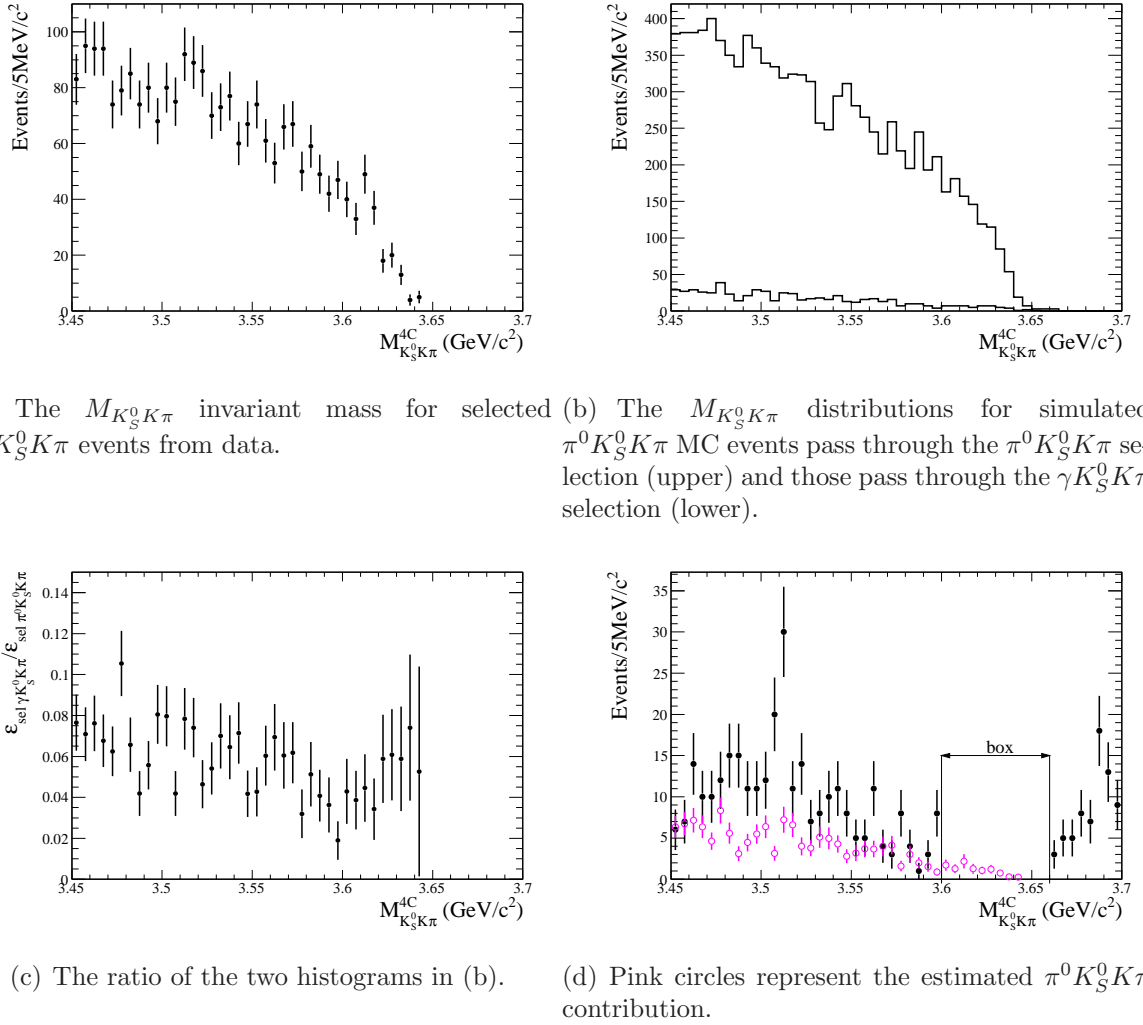


Figure 21: Estimate the $\pi^0 K_S^0 K^\pm \pi^\mp$ background in $\eta_c(2S)$ mass region.

The mass of $K_S^0 K^\pm \pi^\mp$ for selected $\pi^0 K_S^0 K^\pm \pi^\mp$ events is still calculated in the same way as $\gamma K_S^0 K^\pm \pi^\mp$ selection, which is shown in Fig. 21(a). According to the simulation with large statistics for $e^+e^- \rightarrow \pi^0 K_S^0 K^\pm \pi^\mp$ MC sample, the $M_{K_S^0 K \pi}^{4C}$ distribution for events passing through the $\pi^0 K_S^0 K^\pm \pi^\mp$ selection (the upper histogram) and the $M_{K_S^0 K \pi}^{4C}$ distribution for events passing through the $\gamma K_S^0 K^\pm \pi^\mp$ selection (the lower histogram) are obtained as shown in Fig. 21(b) and the efficiency ratio of the two event selections f_{scale} (the selections for $\gamma K_S^0 K^\pm \pi^\mp$ and $\pi^0 K_S^0 K^\pm \pi^\mp$) as a function of $M_{K_S^0 K \pi}^{4C}$ is shown in Fig. 21(c). Finally, the contaminated mass

spectrum comes from $\pi^0 K_S^0 K^\pm \pi^\mp$ background is estimated by scaling the measured mass spectrum with the efficiency ratio spectrum. As shown in Fig. 21(d), the mass spectrum for the background from $\pi^0 K_S^0 K^\pm \pi^\mp$ distributes smoothly without special structure.

7.1.3 Background from $K_S^0 K^\pm \pi^\mp (\gamma_{ISR}/\gamma_{FSR})$

As the energy of the transition photon for $\psi(3770) \rightarrow \gamma \eta_c(2S)$ is about 130 MeV, which is so soft that the events from $e^+e^- \rightarrow (\gamma) K_S^0 K^\pm \pi^\mp$ can contaminate the signal by fake photons or real soft photons from FSR or ISR. We use the same method as introduced in Section 6.1.3 to estimate the contribution of this background. The final mass spectrum for $e^+e^- \rightarrow (\gamma) K_S^0 K^\pm \pi^\mp$ MC is shown in Fig. 22 (the mass above 3.45 GeV/c^2), where the photons from FSR are generated by PHOTOS [18] and the photons from ISR are generated by ConExc. According to the plot, the FSR events dominate in $\eta_c(2S)$ mass region.

The invariant mass spectrum of $K_S^0 K^\pm \pi^\mp$ in $\eta_c(2S)$ mass region and the summed mass spectrum of all the estimated backgrounds are shown in Fig. 23, where that the estimated backgrounds can describe data well. It indicates that the estimation of backgrounds is reliable. An additional explanation is necessary here: the component of $e^+e^- \rightarrow (\gamma) K_S^0 K^\pm \pi^\mp$ estimated by MC is normalized to data according to the generated cross section of MC sample.

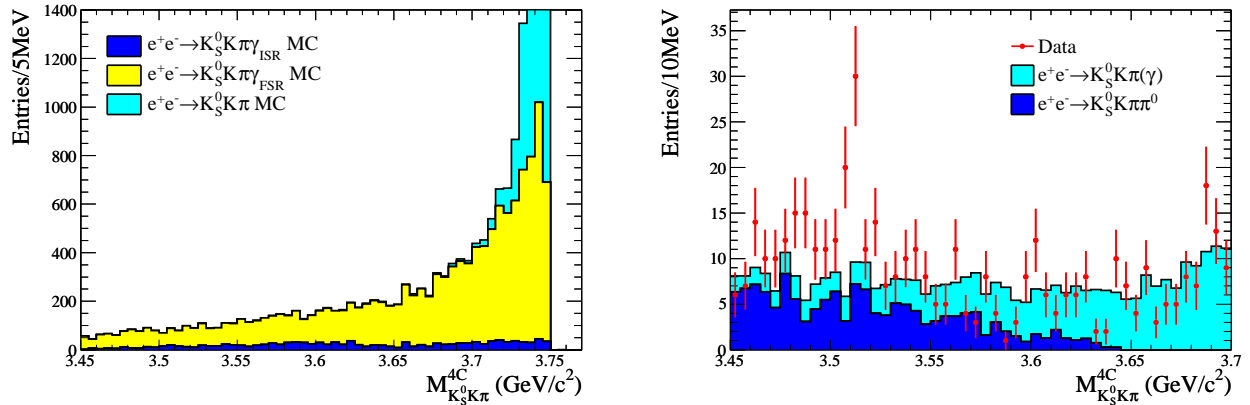


Figure 22: The invariant mass distribution of $K_S^0 K^\pm \pi^\mp$ for $e^+e^- \rightarrow (\gamma) K_S^0 K^\pm \pi^\mp$ MC.

Figure 23: The invariant mass spectrum of $K_S^0 K^\pm \pi^\mp$ in $\eta_c(2S)$ mass region and the summed mass spectrum of all the estimated backgrounds.

7.1.4 Background from $\psi(3686)$ tail

A kind of peaking background source is the tail of the $\psi(3686)$ resonance produced at the resonance energy $\sqrt{s} = 3.773$ GeV as the same case as Section 6.1.4. To get the number of $\psi(3686) \rightarrow \gamma \eta_c(2S), \gamma \chi_{c1}$ signal events, the number of the background events of $\psi(3686) \rightarrow \gamma \eta_c(2S), \gamma \chi_{c1}$ has to be subtracted from the number of observed candidate events of $\gamma \eta_c(2S)$ and $\gamma \chi_{c1}$. By inserting the corresponding numbers in Eq. 3, we can obtain the number of the background events from the $\psi(3686)$ decays at $\sqrt{s} = 3.773$ GeV, as shown in Table 7. The errors arise from the uncertainties in \mathcal{L} , $\sigma_{\psi(3686)}$, ϵ and \mathcal{B}_i .

Table 7: The number of the background events from the $\psi(3686)$ decays at $\sqrt{s} = 3.773$ GeV.

X	$\mathcal{L}[fb^{-1}]$	$\sigma_{\psi'}[nb]$	ϵ	$\mathcal{B}(\psi' \rightarrow \gamma X, X \rightarrow K_S^0 K \pi)$	$\mathcal{B}(K_S^0 \rightarrow \pi^+ \pi^-)[\%]$	$N_{\psi'}^b$
$\eta_c(2S)$	2.92	0.025	0.256	$(4.31 \pm 0.75) \times 10^{-6}$	69.20 ± 0.05	< 0.1
χ_{c1}	2.92	0.025	0.293	$(3.44 \pm 0.32) \times 10^{-4}$	69.20 ± 0.05	5.0 ± 0.6

7.1.5 Potential peaking background check

In addition to the above sources of background, we also check whether other processes could contaminate the signal events by analyzing the corresponding inclusive MC samples generated at the center-of-mass energy 3.773 GeV described in Section 3.2. Fig. 24 show the distributions of the invariant mass $M_{K_S^0 K \pi}^{4C}$ for the $D\bar{D}$, non- $D\bar{D}$, ISR J/ψ , ISR $\psi(3686)$, $\tau^+ \tau^-$ and $q\bar{q}$ inclusive MC samples, respectively, which are normalized to the luminosity of real data. We found that only ISR $\psi(3686)$ events make up a peak in χ_{c1} mass region which needs to be studied.

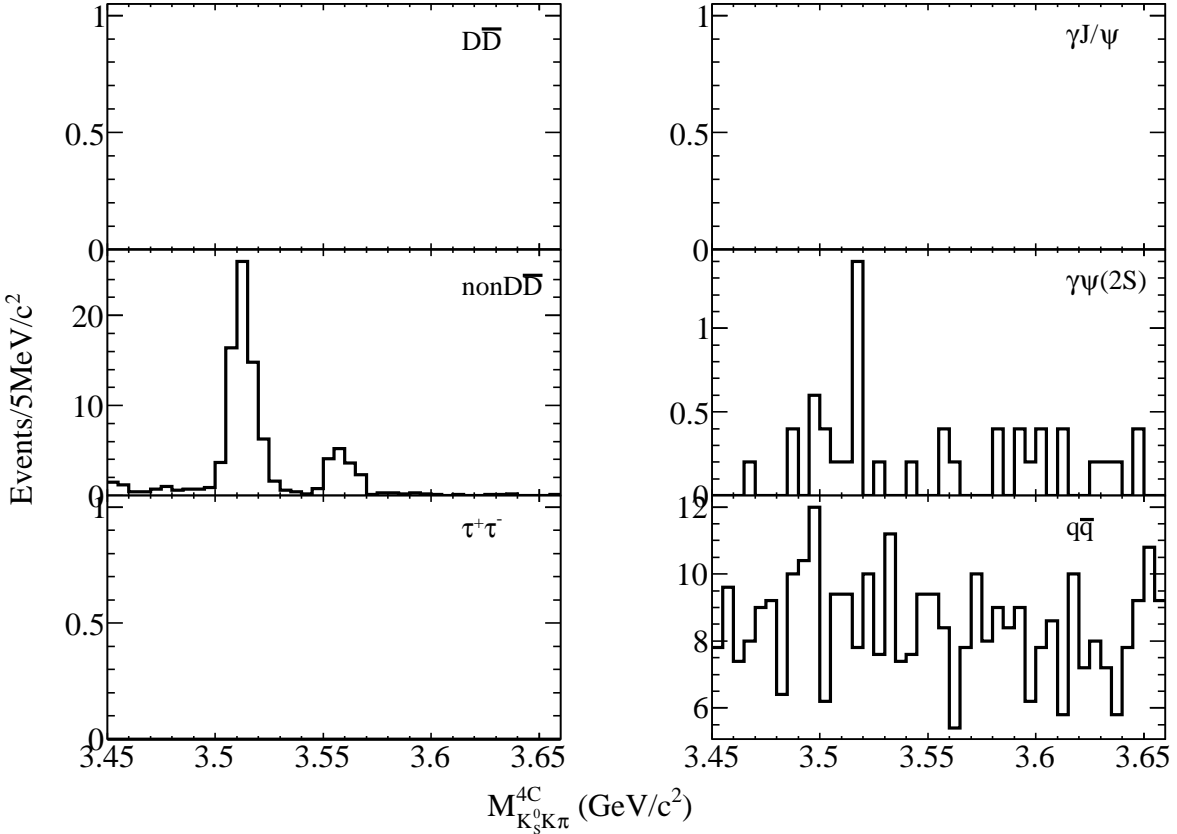


Figure 24: The distributions of $M_{K_S^0 K \pi}^{4C}$ for the surviving background events selected from $D\bar{D}$, ISR J/ψ , non- $D\bar{D}$, ISR $\psi(3686)$, $\tau^+ \tau^-$ and $q\bar{q}$ MC samples, respectively.

The peaking background contribution is found coming from the process $e^+ e^- \rightarrow \gamma_{\text{ISR}} \psi(3686)$,

$\psi(3686) \rightarrow \gamma\chi_{c1} \rightarrow \gamma K_S^0 K^\pm \pi^\mp$ by further studying ISR $\psi(3686)$ MC sample. This background is reduced by the χ_{4C}^2 requirement, but cannot be further suppressed without hurting the sensitivity significantly. Using the detection efficiency determined from MC simulation, the theoretical cross section for the ISR process $e^+e^- \rightarrow \gamma_{\text{ISR}}\psi(3686)$ at $\sqrt{s} = 3.773$ GeV, and the corresponding branching fractions from previous measurements [16], the background contribution from this peaking background channel is estimated to be 1.4 ± 0.2 in the fitting range ($3.45\text{-}3.71$ GeV/c^2). The line shape of this peaking background, as shown in Fig. 25, is extracted from MC simulation, which will be included in the fit.

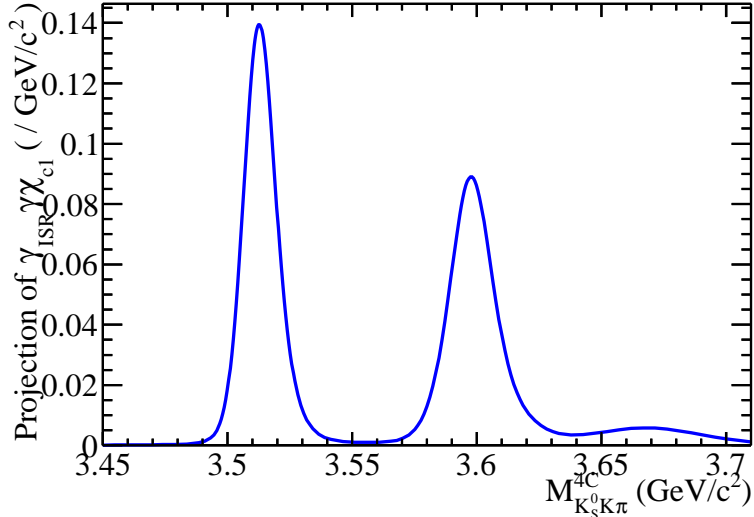


Figure 25: The line shape of the peaking background from $e^+e^- \rightarrow \gamma_{\text{ISR}}\psi(3686)$, $\psi(3686) \rightarrow \gamma\chi_{c1} \rightarrow \gamma K_S^0 K^\pm \pi^\mp$ extracted from MC sample.

7.2 Mass spectrum fitting results of real data

7.2.1 The detector resolution

The detector resolution is primarily determined by Dalitz distributed MC simulation for $\eta_c(2S)$ and χ_{c1} decay modes with zero natural width, respectively. The consistency/discrepancy between data and MC is studied by using the decay $e^+e^- \rightarrow \gamma(\text{ISR})J/\psi$ with J/ψ decays into the same final states as signal modes by using the same procedures as introduced in Section 6.2.1. Here we assume that the discrepancy is constant over the fitting range or mass-independent.

7.2.2 Fit to the mass spectrum

After applying all the selection criteria discussed above, the invariant mass spectrum $M_{K_S^0 K\pi}^{\text{4C}}$ in 2.92 fb^{-1} data is shown in Fig. 28. In order to determine the background better, the mass spectrum range is enlarged ($3.45 \sim 3.71$ GeV/c^2) to include χ_{c1} and $\psi(3686)$ events.

The line shape for $\eta_c(2S)$ and χ_{c1} signals should be described carefully before the fitting. The fitting probability density function(P.D.F) for both the resonances of $\eta_c(2S)$ and χ_{c1} read:

$$F(m) = \sigma \otimes (\epsilon(m) \times E_\gamma^3 \times f_{\text{damp}}(E_\gamma) \times BW(m)) \quad (5)$$

where m is the invariant mass of $K_S^0 K\pi$; σ is the experimental resolution mentioned in Section 7.2.1; $\epsilon(m)$ is mass-dependent efficiency, shown in Fig. 26, which is determined from the MC sample generated according to Dalitz distribution of $\eta_c(2S)$ decay $\eta_c(2S) \rightarrow K_S^0 K^\pm \pi^\mp$ or χ_{c1} decay $\chi_{c1} \rightarrow K_S^0 K^\pm \pi^\mp$; $BW(m)$ is the relativistic Breit-Wigner formula, the mass and width of η_c , χ_{c1} are fixed to the values of PDG2012 [16]; E_γ^3 is radiative transition form factor where $E_\gamma = \frac{m_{\psi(3770)}^2 - m^2}{2m_{\psi(3770)}}$ is the energy of the transition photon in the rest frame of $\psi(3770)$; $f_{damp}(E_\gamma)$ is the function to damp the diverging tail raise by E_γ^3 . The possible form of the damping function is somewhat arbitrary, and one suitable function used by KEDR for a similar process is [19]:

$$f_{damp}^{\text{KEDR}} = \frac{E_0^2}{E_\gamma E_0 + (E_\gamma - E_0)^2} \quad (6)$$

where $E_0 = \frac{m_{\psi(3770)}^2 - m_{\eta_c(2S)}^2}{2m_{\psi(3770)}}$ or $\frac{m_{\psi(3770)}^2 - m_{\chi_{c1}}^2}{2m_{\psi(3770)}}$ is the peaking energy of the transition photon. Another damping function used by CLEO [20] is inspired by the overlap of wave functions:

$$f_{damp}^{\text{CLEO}} = \exp\left(-\frac{E_\gamma^2}{8\beta^2}\right) \quad (7)$$

with $\beta = (65.0 \pm 2.5)$ MeV from CLEO's fit. In our analysis, the damping function (6) will be used in the fit to give the final results, and the form (7) will be used to estimate the possible uncertainty caused by the form of damping functions.

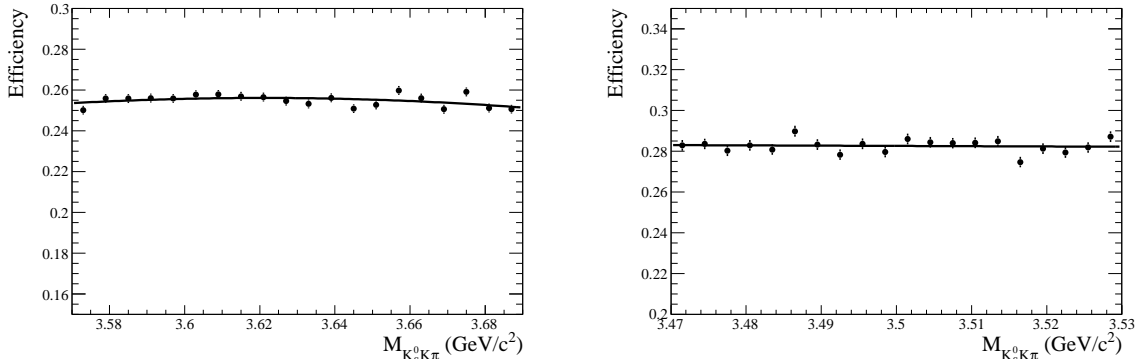


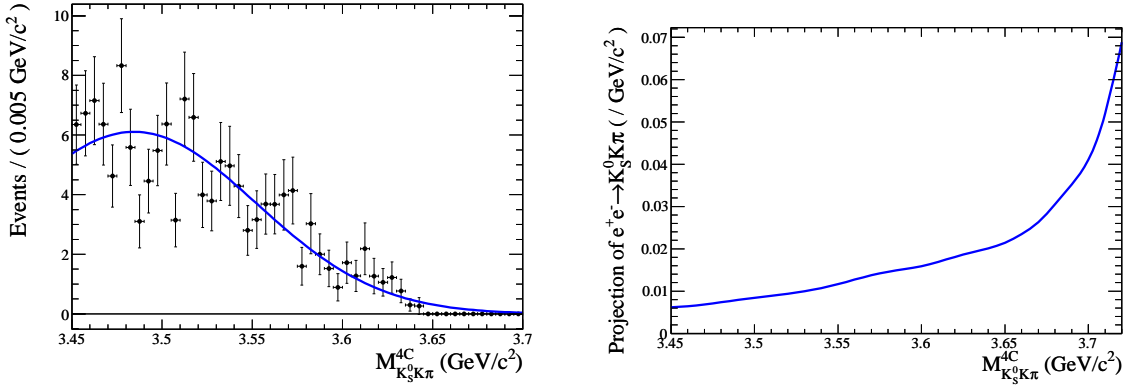
Figure 26: The efficiency as a function of $K_S^0 K^\pm \pi^\mp$ mass. Left: for the $\eta_c(2S)$ signal MC generated by MassH2; Right: for the χ_{c1} signal MC generated by MassH2.

The line shape for $\psi(3686)$ resonance is described by a single Gaussian function with mean value fixed to that of PDG2012 [16]. The background from the lower mass side is dominated by $\pi^0 K_S^0 K^\pm \pi^\mp$ process, which is studied in data (see Section 7.1.2). The line shape of this background can be described by Novosibirsk function. The fitting of the corresponding mass spectrum using this function is shown in Fig. 27(a). The determined shape and number of events for $\pi^0 K_S^0 K^\pm \pi^\mp$ are fixed in the final mass fitting.

The background on the higher mass side is $e^+e^- \rightarrow K_S^0 K^\pm \pi^\mp (\gamma_{ISR}/\gamma_{FSR})$. This process of background has been studied in Section 7.1.3. So we use the shape of the extracted $e^+e^- \rightarrow K_S^0 K^\pm \pi^\mp (\gamma_{ISR}/\gamma_{FSR})$ MC sample (Fig. 27(b)) to describe the line shape of the mass spectrum for the higher side background. The shape for the peaking background $e^+e^- \rightarrow \gamma_{ISR}\psi(3686)$, $\psi(3686) \rightarrow \gamma\chi_{c1} \rightarrow \gamma K_S^0 K^\pm \pi^\mp$ comes from the MC simulation, and its magnitude is fixed to the expected number determined from the background study.

As a short summary, the final function used to fit the data mass spectrum is the sum of the following components:

- $\eta_c(2S)$ & χ_{c1} : a modified theoretical form times efficiency, then convolved with the experimental resolution function (see Eq. 5)
- backgrounds
 - background from $\pi^0 K_S^0 K^\pm \pi^\mp$: a Novosibirsk function, the parameters and number of events are fixed to the fit result shown in Fig. 27(a);
 - background from $K_S^0 K^\pm \pi^\mp (\gamma_{ISR}/\gamma_{FSR})$: MC shape shown in Fig. 27(b), the number of events is floated.
 - background from $e^+ e^- \rightarrow \gamma_{ISR} \psi(3686)$, $\psi(3686) \rightarrow \gamma \chi_{c1} \rightarrow \gamma K_S^0 K^\pm \pi^\mp$: MC shape shown in Fig. 25, the number of events is fixed.



(a) The fitting results of the mass spectrum of $\pi^0 K_S^0 K^\pm \pi^\mp$ background to Novosibirsk function. (b) The line shape of the background from $K_S^0 K^\pm \pi^\mp (\gamma_{ISR}/\gamma_{FSR})$ extracted from MC sample.

Figure 27: The line shape functions for backgrounds used to fit the data mass spectrum.

An unbinned maximum likelihood fit is performed to the full invariant mass spectrum in Fig. 28. The χ^2/ndf is 1.04. The related results are listed in Table 8. 1.4 ± 8.5 $\eta_c(2S)$ signal events, 51.9 ± 9.8 χ_{c1} events, and 13.6 ± 6.9 $\psi(3686)$ events are extracted from the fit. Since there is no significant $\eta_c(2S)$ signal that we can also calculate the upper limit of the $\eta_c(2S)$ signal events by using the Bayesian method. The upper limit of the number of $\eta_c(2S)$ signal events is determined to be 16.7 at 90% C.L. as shown in Fig. 29.

Table 8: Results of the fit to the invariant mass spectrum of $K_S^0 K^\pm \pi^\mp$ in $\eta_c(2S)$ mass region. Errors are only statistical.

$\psi'' \rightarrow \gamma X$	$\eta_c(2S)$	U.L. of $\eta_c(2S)$ (90% C.L.)	χ_{c1}	ψ'	$BG(\pi^0 K_S^0 K\pi)$	$BG(K_S^0 K\pi(\gamma))$
N_{yield}^{data}	1.4 ± 8.5	16.7	51.9 ± 9.8	13.6 ± 6.9	144.2	216.8 ± 22.7

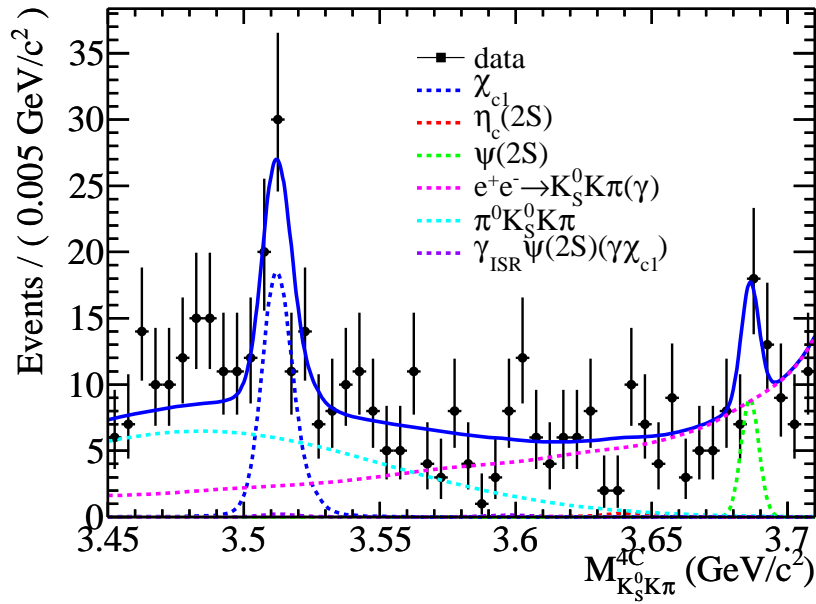


Figure 28: The invariant mass distribution of $K_S^0 K^{\pm} \pi^{\mp}$ in $\eta_c(2S)$ and χ_{c1} mass region for real data. Solid curve shows the result of unbinned maximum likelihood fit.

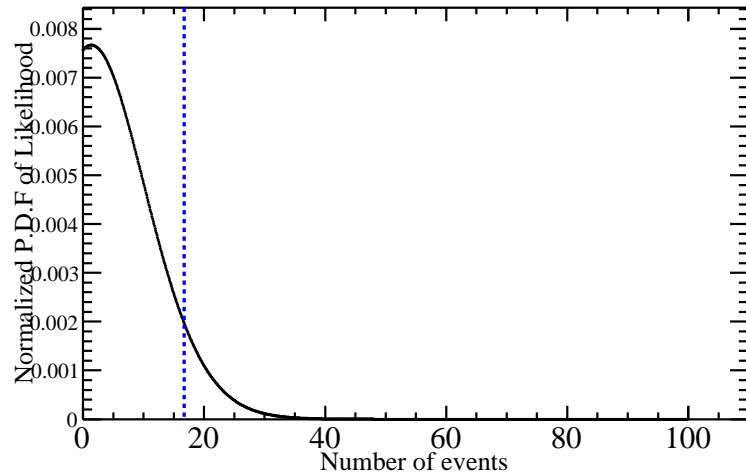


Figure 29: The upper limit of the number of $\eta_c(2S)$ signal events at 90% C.L. from Bayesian approach.

7.2.3 Input/Output check

To check the analysis and fitting method, we have performed a MC Input/Output check. This check is based on the analysis of all kinds of corresponding inclusive MC samples generated at the center-of-mass energy 3.773 GeV (except the process $e^+e^- \rightarrow \gamma(ISR)\psi(3686)$) and a signal MC sample for $\psi(3770) \rightarrow \gamma\eta_c(2S)$, $\eta_c(2S) \rightarrow K_S^0 K^\pm \pi^\mp$ described in Section 3.2. We put these MC samples together with each event weighted. For the inclusive MC samples, the weight factor of each event should be related to the luminosity scale factor of each inclusive MC sample mentioned in Table 2 to make sure that all inclusive MC samples are normalized to data luminosity. The input branching fraction for $\psi(3770) \rightarrow \gamma\eta_c(2S)$ is 6.667×10^{-5} according to the theoretical prediction and that for $\psi(3770) \rightarrow \gamma\chi_{c1}$ is 2.9×10^{-3} extracted from the decay table used in the generation of MC samples.

By using the same analysis procedure and fitting method as data analysis, we obtain the observed numbers of $\eta_c(2S)$ and χ_{c1} as shown in Fig. 30. The comparisons of the input and output signal numbers and relative branching fractions are summarized in Table 9. We can see that the output yields are well consistent with the input value within statistic error.

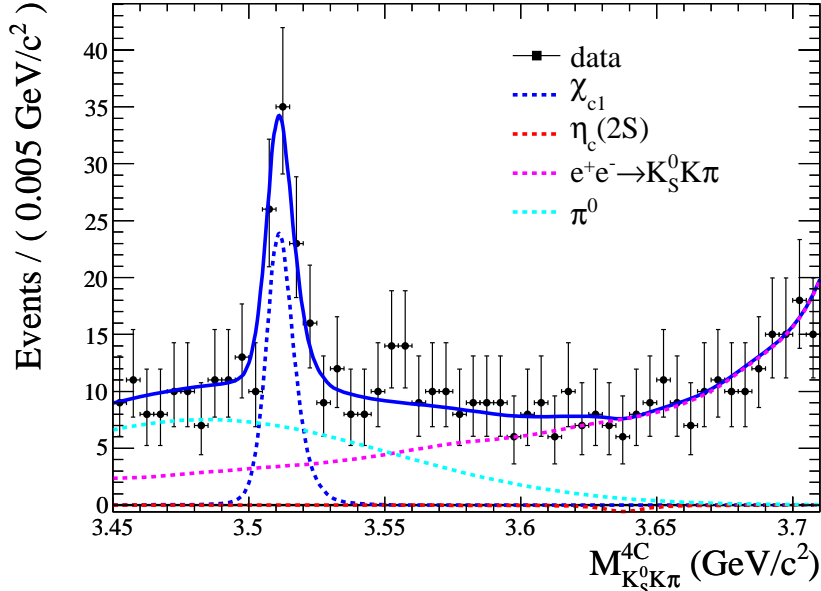


Figure 30: The invariant mass distribution of $K_S^0 K^\pm \pi^\mp$ in $\eta_c(2S)$ mass region for known MC samples. Solid curve shows the result of unbinned maximum likelihood fit.

Table 9: The comparisons of the input and output signal numbers and relative branching fractions.

	$N_{\eta_c(2S)}$	$N_{\chi_{c1}}$	$\mathcal{B}(\psi(3770) \rightarrow \gamma\chi_{c1})$
Input	1.5	68.8	2.9×10^{-3}
Output	-2.7 ± 9.5	64.0 ± 11.2	$(2.70 \pm 0.47) \times 10^{-3}$

8 Systematic uncertainties

The systematic uncertainties of the branching ratios of $\psi(3770)$ to $\gamma\eta_c, \gamma\eta_c(2S)$, $\gamma\chi_{c1}$ and $e^+e^- \rightarrow \gamma_{ISR} J/\psi$ are mainly originated from MDC tracking efficiency, photon detection, K_S^0 reconstruction, kinematic fitting, D^0 and π^0 veto, integrated luminosity of data, cross section for $\psi(3770)$, $K_S^0 K^\pm \pi^\mp$ intermediate states, background shapes, damping function, signal fitting range and so on, which will be discussed in detail in the following subsections.

8.1 Tracking efficiency for π , K from IP

The tracking efficiencies from K_S^0 are already considered in the study of the K_S^0 reconstruction which will be introduced later. This subsection discusses the other two charged tracks directly produced at IP. The efficiencies of the MDC K^\pm and π^\pm tracking at $\sqrt{s} = 3.773$ GeV have been studied by the doubly tagged hadronic decay modes of $D^0 \rightarrow K^-\pi^+$ vs. $\bar{D}^0 \rightarrow K^+\pi^-$ (charge conjugate is implied), $D^0 \rightarrow K^-\pi^+\pi^0$ vs. $\bar{D}^0 \rightarrow K^+\pi^-$, $D^0 \rightarrow K^-\pi^+\pi^+\pi^-$ vs. $\bar{D}^0 \rightarrow K^+\pi^-$, $D^0 \rightarrow K^-\pi^+$ vs. $\bar{D}^0 \rightarrow K^+\pi^-\pi^-\pi^+$, $D^0 \rightarrow K^-\pi^+\pi^0$ vs. $\bar{D}^0 \rightarrow K^+\pi^-\pi^-\pi^+$, $D^0 \rightarrow K^-\pi^+\pi^+\pi^-$ vs. $\bar{D}^0 \rightarrow K^+\pi^-\pi^-\pi^+$ and $D^+ \rightarrow K^-\pi^+\pi^+$ vs. $D^- \rightarrow K^+\pi^-\pi^-$ [21]. The differences of kaon and pion tracking efficiencies between data and MC in different momentum ranges are shown in Fig. 31. The transverse momentum distributions for π and K in the $\psi(3770) \rightarrow \gamma\eta_c \rightarrow \gamma K_S^0 K^\pm \pi^\mp$ MC sample are shown in Fig. 32. The difference in efficiencies between data and MC results in 1% for each π or K track. So 2-track uncertainty is 2% which is taken as the uncertainty of tracking efficiency of this analysis.

8.2 Photon detection efficiency

The systematic uncertainty due to photon reconstruction is estimated to be 1% per photon [22]. This is derived from a series of studies on photon detection in the well understood channels: $J/\psi \rightarrow \rho^0 \pi^0, \rho^0 \rightarrow \pi^+ \pi^-, \pi^0 \rightarrow \gamma\gamma$ and study of photon conversion via $e^+e^- \rightarrow \gamma\gamma$ provided by Data Quality/Validation group.

8.3 Efficiency for K_S^0 reconstruction

Three parts contribute to the complete efficiency for K_S^0 reconstruction: the geometric acceptance, tracking efficiency and the efficiency of K_S^0 selection. The first part can be estimated using MC sample. The other two were studied by the doubly tagged hadronic decay modes of $D^0 \rightarrow K_S^0 \pi^+\pi^-$ vs. $\bar{D}^0 \rightarrow K^+\pi^-$, $D^0 \rightarrow K_S^0 \pi^+\pi^-$ vs. $\bar{D}^0 \rightarrow K^+\pi^-\pi^0$, and $D^0 \rightarrow K_S^0 \pi^+\pi^-$ vs. $\bar{D}^0 \rightarrow K^+\pi^-\pi^-\pi^+$ (under Boss 6.6.2) [23] and the process $J/\psi \rightarrow K^* \bar{K}^0 + c.c.$ (under Boss

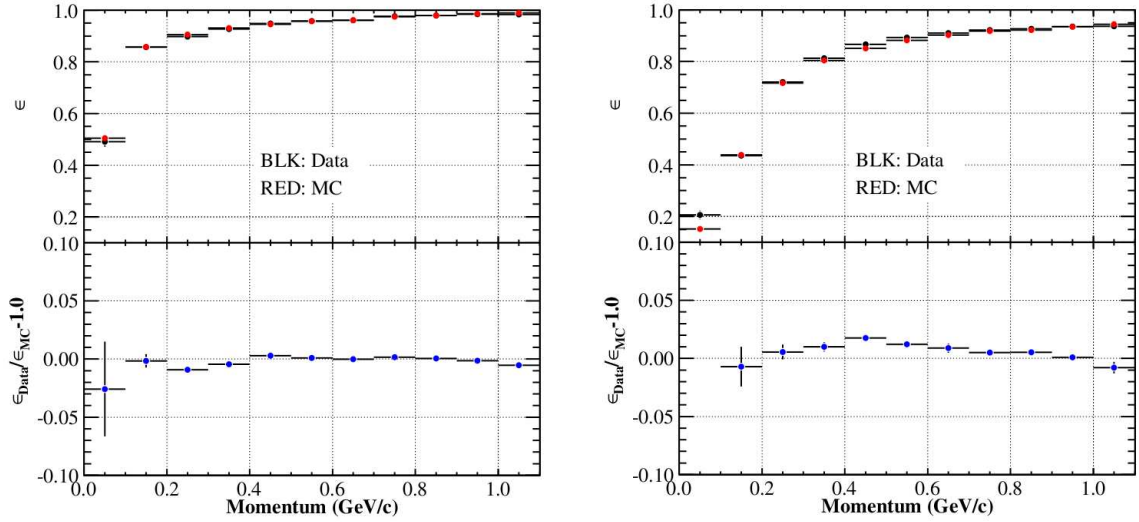


Figure 31: The difference in the tracking efficiency between data and MC as a function of transverse momentum for pions (left) and kaons (right).

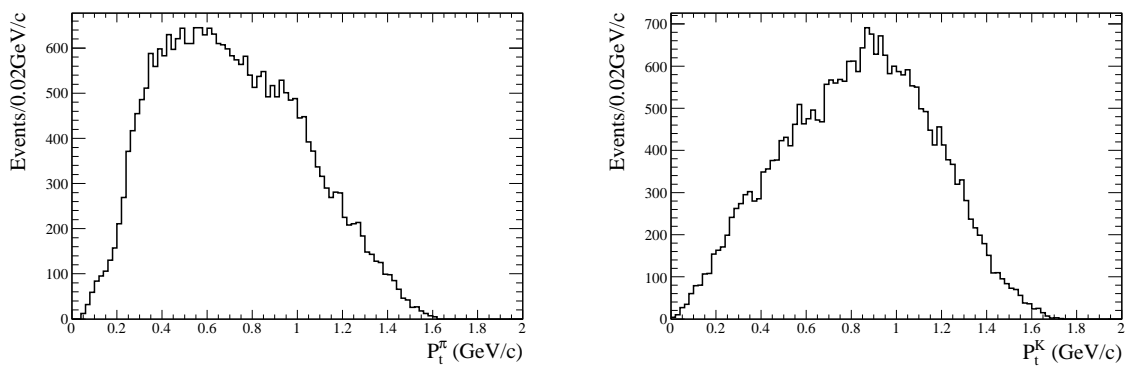


Figure 32: The transverse momentum distributions for π (left) and K (right) in the $\psi(3770) \rightarrow \gamma\eta_c \rightarrow \gamma K_S^0 K^\pm \pi^\mp$ MC sample.

6.5.5) [24]. With these two samples, one can check the possibility to reconstruct the K_S^0 from a pair of pions. The difference between data and MC is found to be 4.0%.

8.4 Efficiency for χ^2 cut of kinematic fitting

From most analyses we can see obvious difference between MC and data on the distribution of χ_{4C}^2 and pulls. The traditional method is using control samples to estimate the systematic error of this difference. But this method has some disadvantages. Firstly, for most channels it is hard to find appropriate reference channel with the final states and momentum distributions similar to the analysis process; furthermore, it is difficult to select pure control sample without using kinematic constraints or selection criteria correlated with kinematic constraints such as total energy, total momentum and so on. The method used in this analysis is to correct the track helix parameters ($\phi_0, \kappa, \tan \lambda$) to reduce the difference between MC and data. We use $J/\psi \rightarrow \phi f_0(980), \phi \rightarrow K^+ K^-, f_0(980) \rightarrow \pi^+ \pi^-$ as control sample to extract correction factors [25] from pull distributions. The correction factors are listed in Table 10. The MC samples after correction are used to estimate the efficiency and fit the invariant mass spectrum.

If the correction is perfect, the difference between MC and data on the distribution of χ_{4C}^2 is negligible and the systematic error comes from the uncertainty of the correction factors. After correction, the difference between MC and data reduced obviously and the distributions of χ_{4C}^2 for MC and data match well. The suggested value of the uncertainty is the difference on the efficiency between MC before and after correction as a conservative estimation. The comparison of χ_{4C}^2 between MC and data with and without correction for the reference channel $e^+ e^- \rightarrow \gamma_{ISR} J/\psi, J/\psi \rightarrow K_S^0 K^\pm \pi^\mp$ are shown in Fig. 33, and the total efficiencies for the channels of interest before and after correction are summarized in Table 11.

Table 10: Correction factors extracted from pull distributions.

	ϕ_0		κ		$\tan \lambda$	
	$m^{data} - m^{MC}$	$\sigma^{data}/\sigma^{MC}$	$m^{data} - m^{MC}$	$\sigma^{data}/\sigma^{MC}$	$m^{data} - m^{MC}$	$\sigma^{data}/\sigma^{MC}$
K^+	–	1.18	–	1.27	–	1.14
K^-	–	1.19	–	1.24	–	1.11
π^+	–	1.25	–	1.25	–	1.15
π^-	–	1.22	–	1.23	–	1.13

Table 11: Summary of efficiencies after final selection with and without correction.

Decay mode	$\psi'' \rightarrow \gamma \eta_c$	$e^+ e^- \rightarrow \gamma_{ISR} J/\psi$	$\psi'' \rightarrow \gamma \eta_c(2S)$	$\psi'' \rightarrow \gamma \chi_{c1}$
Without correction	28.97%	6.13%	26.63%	29.98%
With correction	27.87%	5.89%	25.24%	28.46%
Systematic error	3.9%	4.1%	5.5%	5.3%

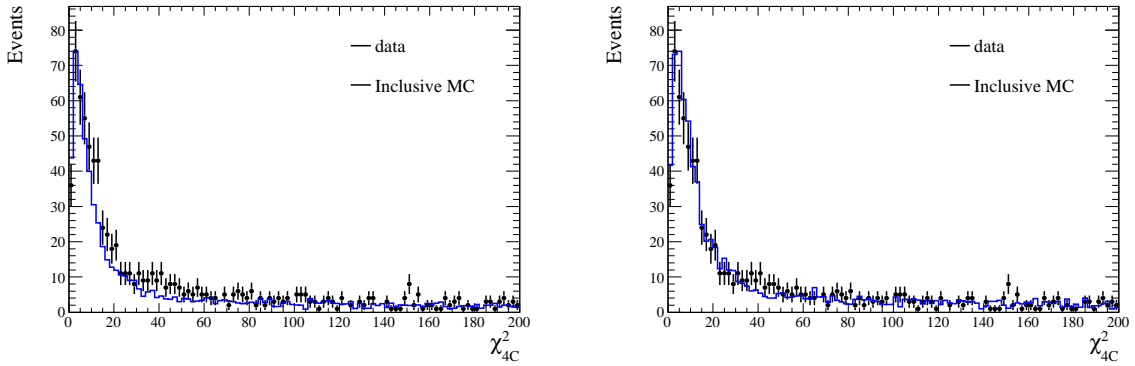


Figure 33: The comparison of χ^2_{4C} between MC and data for $e^+e^- \rightarrow \gamma_{ISR} J/\psi, J/\psi \rightarrow K_S^0 K^\pm \pi^\mp$. Left: MC without correction; Right: MC with correction.

8.5 Efficiency for D^0 and π^0 veto

The systematic uncertainty of the efficiency caused by D^0 veto ($|m_{K^\pm \pi^\mp} - m_{D^0}| > 3\sigma$) and π^0 veto ($\chi^2_{4C}(\gamma K_S^0 K^\pm \pi^\mp) < \chi^2_{4C}(\gamma \gamma K_S^0 K^\pm \pi^\mp)$) cuts is studied with control sample: $e^+e^- \rightarrow \gamma_{ISR} J/\psi, J/\psi \rightarrow K_S^0 K^\pm \pi^\mp$. Here we combine these two selections together to estimate the systematic error. This systematic error is estimated by comparing the differences of efficiencies between data and MC with and without D^0 & π^0 veto cuts.

The selection criteria for this control sample are exactly the same as the analysis described above except the D^0 & π^0 veto cuts which are investigated. Since we cannot pick out a pure control sample, an unbinned likelihood fit is performed to the invariant mass spectrum $M_{K_S^0 K\pi}^{4C}$ to obtain the signal and background's yield. In the fit, the line shape of J/ψ is described by a single Gaussian function with free parameters, while the background is described using a 1st order Chebychev polynomial. Figure 34 shows the fitting results of data and MC simulation with and without D^0 & π^0 veto cuts. The efficiency of D^0 and π^0 veto for data and MC is determined to be $(95.67 \pm 1.07)\%$ and $(97.75 \pm 0.19)\%$, respectively. To be conservative, 3.2% is taken as the systematic error for the efficiency of D^0 and π^0 veto.

8.6 Integrated luminosity of data

By analyzing the Bhabha scattering events from the data taken at $\sqrt{s} = 3.773$ GeV, L.L. Jiang and her colleagues determine the integrated luminosity of the data to be 2.92 fb^{-1} , where, the statistical error can be negligible, and the systematic error is 1.0% [17].

8.7 Cross section of $\psi(3770)$

To determine the total number of $\psi(3770)$, we use the so-called Born-level cross section of $\psi(3770)$ at $\sqrt{s} = 3.773$ GeV, $\sigma_{\psi(3770)}^0 = (9.93 \pm 0.77) \text{ nb}$, which is calculated by the relativistic Breit-Wigner formula with the $\psi(3770)$ resonance parameters [16]. The uncertainty of $\sigma_{\psi(3770)}^0$ is 7.8% arising dominantly from the errors in $\psi(3770)$ resonance parameters.

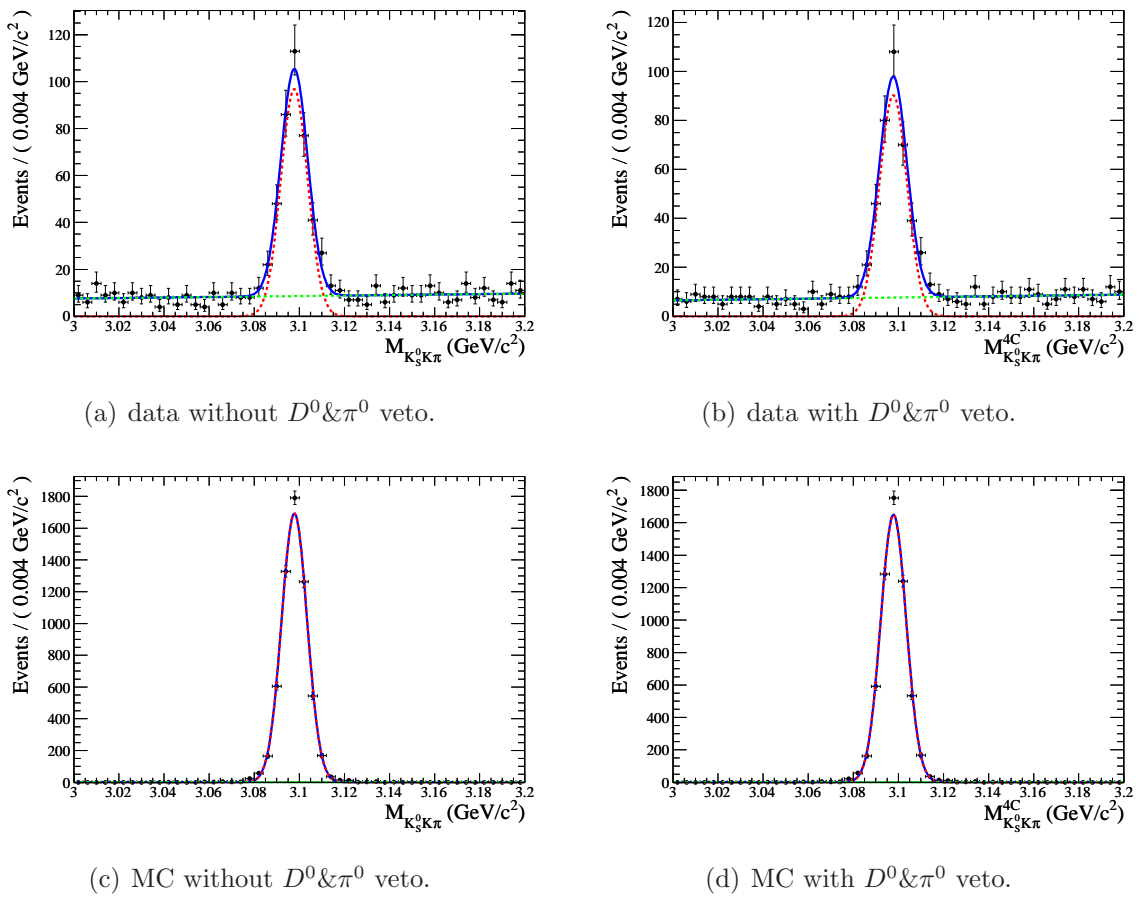


Figure 34: The fitting results of data and MC simulation with and without $D^0 \& \pi^0$ veto cuts.

8.8 Possible intermediate states

The decays $\eta_c, \eta_c(2S), \chi_{c1}, J/\psi \rightarrow K_S^0 K^\pm \pi^\mp$ are simulated based on the Dalitz distributions of final states by using the generator MassH2 in our standard signal MC samples. The Dalitz distributions of $\eta_c \rightarrow K_S^0 K^\pm \pi^\mp$, $\chi_{c1} \rightarrow K_S^0 K^\pm \pi^\mp$, and $J/\psi \rightarrow K_S^0 K^\pm \pi^\mp$, are shown in Fig. 35(e), Fig. 35(g), and Fig. 35(h), which are obtained by studying the processes $\psi' \rightarrow \gamma \eta_c(\chi_{c1}), \eta_c(\chi_{c1}) \rightarrow K_S^0 K^\pm \pi^\mp$ and $J/\psi \rightarrow K_S^0 K^\pm \pi^\mp$, respectively. The recent analysis gives the Dalitz plot (Fig. 35(f)) of $\eta_c(2S) \rightarrow K_S^0 K^\pm \pi^\mp$ via searching the process $B^\pm \rightarrow K^\pm \eta_c(2S) \rightarrow K^\pm (K_S^0 K^\pm)^\pm$ by Belle Collaboration [28]. The components of the intermediate states are likely $K_0^*(1430)\bar{K}$, $K_2^*(1430)\bar{K}$, $a_0(980)^\pm \pi^\mp$, $a_2(1320)^\pm \pi^\mp$ and $K^*(892)\bar{K}$. The efficiencies obtained by the simulations with these Dalitz distributions of final states are taken as the central values. However, there still exists a possible systematic bias from the generation of the signal MC samples. So that alternative signal MC samples (The decays $\eta_c, \eta_c(2S), \chi_{c1} \rightarrow K_S^0 K^\pm \pi^\mp$ are treated as phase space. However, we take the process $J/\psi \rightarrow K\bar{K}^*(892) + c.c. \rightarrow K_S^0 K^\pm \pi^\mp$ which includes the intermediate states $K^*(892)^\pm, K^*(892)^0$ to generate signal events for $e^+e^- \rightarrow \gamma_{ISR} J/\psi, J/\psi \rightarrow K_S^0 K^\pm \pi^\mp$, since we have already known the dominant intermediate states in the decay $J/\psi \rightarrow K_S^0 K^\pm \pi^\mp$.) are generated to estimate the uncertainties from the intermediate states. The differences between efficiencies obtained with two different generator models are taken as the systematic errors due to possible intermediate states. The results are summarized in Table 12.

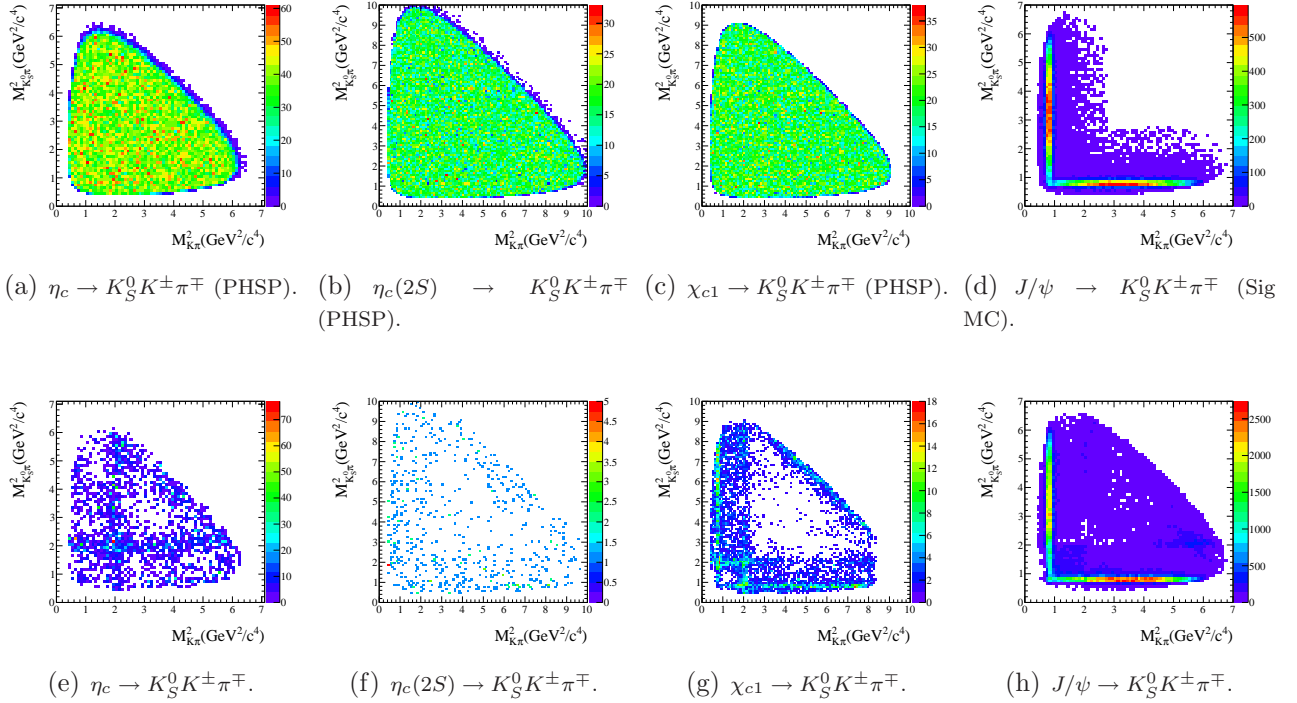


Figure 35: The Dalitz distributions for the decay $\eta_c, \eta_c(2S), \chi_{c1}, J/\psi \rightarrow K_S^0 K^\pm \pi^\mp$.

8.9 Fitting in η_c & J/ψ mass region

For the decay mode $\psi(3770) \rightarrow \gamma \eta_c$, the uncertainty sources from fitting consists of fitting range, background shape and the uncertainties of the mean and width of η_c . Using Bayesian

Table 12: The comparison of efficiencies between different generator models.

Decay mode	$\eta_c \rightarrow K_S^0 K^\pm \pi^\mp$	$\eta_c(2S) \rightarrow K_S^0 K^\pm \pi^\mp$	$\chi_{c1} \rightarrow K_S^0 K^\pm \pi^\mp$	$J/\psi \rightarrow K_S^0 K^\pm \pi^\mp$
Dalitz	27.87%	25.24%	28.46%	5.89%
Sig MC	27.34%	24.40%	27.88%	5.70%
Systematic error	1.9%	3.3%	2.0%	3.2%

method, the upper limit of N_{signal} is calculated in the following situations, and the maximum of the series of N_{signal} is taken as $N_{signal}^{\text{U.L.}}$ conservatively. The upper limits in different situations are listed in Table 13, from which we take 58.4 as the upper limit number. After deducting the peaking background using the method described in Section 6.2.2, we obtain 57.2 as the upper limit number of η_c signal at 90% C.L.

For the decay mode $e^+e^- \rightarrow \gamma_{ISR} J/\psi$, the uncertainty due to the fitting range and the description of background shape is estimated by the difference of signal yields of fitting with various combinations of fitting ranges and background parameterizations (Table 13). The maximum difference of the fitting yield is taken as the systematic uncertainty.

- Fitting region: fitting the invariant mass spectrum in [2.725,3.175] GeV/c^2 , [2.7,3.2] GeV/c^2 and [2.675,3.225] GeV/c^2 .
- Signal line shape: the η_c signal is described by Eq. 4 with the parameters of η_c fixed to the latest PDG value. The uncertainty on the measurement of the mean and width of η_c is estimated by changing the mean and width with one standard deviation respectively.
- Background line shape: using 2nd order Chebychev polynomial and 3rd order Chebychev polynomial to describe the background.

8.10 Fitting in χ_{c1} & $\eta_c(2S)$ mass region

For the decay modes $\psi(3770) \rightarrow \gamma \eta_c(2S)$, χ_{c1} , the uncertainty sources from fitting consists of fitting range, background shape, damping function and the uncertainties of the mean and width of $\eta_c(2S)$ which are discussed as the following:

- Fitting region:
The fitting range has been varied from [3.45,3.71] GeV/c^2 to [3.46,3.70] GeV/c^2 and [3.44,3.72] GeV/c^2 , and the biggest changes on the branching fraction of $\psi(3770) \rightarrow \gamma \chi_{c1}$ or upper limit of the branching fraction of $\psi(3770) \rightarrow \gamma \eta_c(2S)$ have been taken as the systematic errors due to fitting range.
- Mass and width of $\eta_c(2S)$:
The $\eta_c(2S)$ signal is described by Eq. 5 with the parameters of $\eta_c(2S)$ fixed to the latest PDG value. The uncertainty on the measurement of the mean and width of $\eta_c(2S)$ is estimated by changing the mean and width with one standard deviation respectively, and the biggest change on the upper limit of $\eta_c(2S)$ signal is taken as the systematic error.

Table 13: Upper limit of the number of signal events for $\psi(3770) \rightarrow \gamma\eta_c, \eta_c \rightarrow K_S^0 K^\pm \pi^\mp$ and signal yields for $e^+e^- \rightarrow \gamma_{ISR} J/\psi, J/\psi \rightarrow K_S^0 K^\pm \pi^\mp$ when fitting in different situations.

Situations	$N_{\eta_c}^{\text{U.L.}}$	$N_{J/\psi}$
2^{nd} order Chebychev and [2.725,3.175] GeV/c^2	48.2	346.9 ± 20.9
2^{nd} order Chebychev and [2.7,3.2] GeV/c^2	47.6	345.4 ± 20.8
2^{nd} order Chebychev and [2.675,3.225] GeV/c^2	41.7	347.6 ± 20.7
3^{rd} order Chebychev and [2.725,3.175] GeV/c^2	58.4	350.3 ± 21.1
3^{rd} order Chebychev and [2.7,3.2] GeV/c^2	56.8	349.7 ± 21.0
3^{rd} order Chebychev and [2.675,3.225] GeV/c^2	45.3	349.1 ± 21.0
no efficiency curve	56.8	349.7 ± 21.0
mean of η_c : (2981.0+1.1) MeV/c^2	57.8	349.8 ± 21.0
mean of η_c : (2981.0-1.1) MeV/c^2	55.7	349.5 ± 21.0
width of η_c : (29.7+1.0) MeV/c^2	57.4	349.7 ± 21.0
width of η_c : (29.7-1.0) MeV/c^2	56.1	349.7 ± 21.0

- Background line shape:
 - Background from $\pi^0 K_S^0 K^\pm \pi^\mp$:
We vary the fixed number of $\pi^0 K_S^0 K^\pm \pi^\mp$ component in the fit by $\pm 1\sigma$ to consider the uncertainty from magnitude of the $\pi^0 K_S^0 K^\pm \pi^\mp$ background. To estimate the uncertainty caused by the line shape of $\pi^0 K_S^0 K^\pm \pi^\mp$ background, we change the fixed parameters of the P.D.F by $\pm 1\sigma$, and the changes on $N_{\eta_c}^{\text{U.L.}}$ and $N_{\chi_{c1}}$ are taken as the systematic errors.
- Damping function:
This uncertainty is estimated by changing the damping function form from (6) to (7).

8.11 Background from $\psi(3686)$ tail

In the estimation of background contribution from $\psi(3686)$ tail, we use the standard Breit-Wigner formula to express the Born cross section of $\psi(3686)$ at $\sqrt{s} = 3.773 \text{ GeV}$, which is a subjective assumption without theoretical justification. Conservatively, we take the difference between the results with and without subtracting this peaking background as the corresponding systematic uncertainty.

8.12 Total systematic error

The systematic errors for all channels analyzed in this memo are summarized in Table 14. The total systematic error is calculated by combining the uncertainties from all sources in quadrature.

Table 14: Summary of systematic errors for all channels (%).

Source of uncertainties	$\gamma\eta_c$	$\gamma_{ISR} J/\psi$	$\gamma\eta_c(2S)$	$\gamma\chi_{c1}$
Tracking	2.0	2.0	2.0	2.0
Photon reconstruction	1.0	1.0	1.0	1.0
K_S^0 reconstruction	4.0	4.0	4.0	4.0
Kinematic fitting	3.9	4.1	5.5	5.3
$D^0 \& \pi^0$ veto	3.2	3.2	3.2	3.2
$\mathcal{L}_{\psi(3770)}$	1.0	1.0	1.0	1.0
$\sigma_{\psi(3770)}^0 / \sigma_{e^+e^- \rightarrow \gamma J/\psi}$	7.8	3.2	7.8	7.8
$K_S^0 K^\pm \pi^\mp$ intermediate states	1.9	3.2	3.3	2.0
BG line shape	-	1.2	9.4	5.6
Damping function	-	-	2.4	0.2
Fitting range	-	-	8.4	2.9
Number of π^0	-	-	3.0	2.1
Mass and width of $\eta_c(2S)$	-	-	12.3	-
Background from $\psi(3686)$ tail	2.1	-	-	10.7
total	10.8	8.4	21.4	16.8

9 Results and discussion

Here we should point out that we won't consider the interference between signal events and those who have the same final states as a resonant decay but do not include a charmonium resonance. From the whole analysis, we can obtain the upper limits of the product branching ratios for $\psi(3770) \rightarrow \gamma\eta_c, \eta_c \rightarrow K_S^0 K^\pm \pi^\mp$ and $\psi(3770) \rightarrow \gamma\eta_c(2S), \eta_c(2S) \rightarrow K_S^0 K^\pm \pi^\mp$ which are determined by:

$$\mathcal{B}(\psi(3770) \rightarrow \gamma\eta_c/\eta_c(2S)) \mathcal{B}(\eta_c/\eta_c(2S) \rightarrow K_S^0 K^\pm \pi^\mp) < \frac{N_{\text{U.L.}} / (1 - \sigma_{\text{syst.}})}{\epsilon \cdot \mathcal{L} \cdot \sigma_{\psi(3770)}^0 \cdot (1 + \delta) \cdot \mathcal{B}(K_S^0 \rightarrow \pi^+ \pi^-)} \quad (8)$$

where $N_{\text{U.L.}}$ is the upper limit number of signal, $\sigma_{\text{syst.}}$ is the total systematic error, ϵ is the efficiency of the event selection from full simulation, \mathcal{L} is the integrated luminosity of data, $\sigma_{\psi(3770)}^0$ is the Born-level cross section for $\psi(3770)$ produced at 3.773 GeV, $(1 + \delta) = 0.718$ is the radiative correction factor, obtained from the KKMC generator with the $\psi(3770)$ resonance parameters [16] as input, and $\mathcal{B}(K_S^0 \rightarrow \pi^+ \pi^-)$ is the branching ratio for $K_S^0 \rightarrow \pi^+ \pi^-$. And we obtain the branching ratio for $\psi(3770) \rightarrow \gamma\chi_{c1}$ derived from:

$$\mathcal{B}(\psi(3770) \rightarrow \gamma\chi_{c1}) = \frac{N_{\chi_{c1}}}{\epsilon \cdot \mathcal{L} \cdot \sigma_{\psi(3770)}^0 \cdot (1 + \delta) \cdot \mathcal{B}(\chi_{c1} \rightarrow K_S^0 K^\pm \pi^\mp) \cdot \mathcal{B}(K_S^0 \rightarrow \pi^+ \pi^-)} \quad (9)$$

where $\mathcal{B}(\chi_{c1} \rightarrow K_S^0 K^\pm \pi^\mp) = (3.65 \pm 0.30) \times 10^{-3}$ is taken from PDG2012 [16]. Meanwhile, we also give the branching ratio for $J/\psi \rightarrow K_S^0 K^\pm \pi^\mp$ using the following equation:

$$\mathcal{B}(J/\psi \rightarrow K_S^0 K^\pm \pi^\mp) = \frac{N_{J/\psi}}{\epsilon \cdot \mathcal{L} \cdot \sigma_{e^+e^- \rightarrow \gamma J/\psi} \cdot \mathcal{B}(K_S^0 \rightarrow \pi^+ \pi^-)} \quad (10)$$

where $\sigma_{e^+e^-\rightarrow\gamma J/\psi} = 1.02 \pm 0.03$ nb is the cross section for the ISR process $e^+e^- \rightarrow \gamma J/\psi$ at the center-of-mass energy of 3.773 GeV which is determined with the relation [29]:

$$\sigma_{e^+e^-\rightarrow\gamma V} = \int dm \frac{2m}{s} W(s, x) \sigma_0(m), \quad (11)$$

where m is the mass of the vector resonance, and $x \equiv 2E_\gamma/\sqrt{s} = 1 - m^2/s$, $W(s, x)$ is radiator function by taking into consideration of the leading second order correction. The detailed information for this calculation is described in Appendix A. So the final results of the measurement are:

- $\mathcal{B}(\psi(3770) \rightarrow \gamma\eta_c)\mathcal{B}(\eta_c \rightarrow K_S^0 K^\pm \pi^\mp) < 1.6 \times 10^{-5}$ @ 90% C.L.
- $\mathcal{B}(\psi(3770) \rightarrow \gamma\eta_c(2S))\mathcal{B}(\eta_c(2S) \rightarrow K_S^0 K^\pm \pi^\mp) < 5.8 \times 10^{-6}$ @ 90% C.L.
- $\mathcal{B}(\psi(3770) \rightarrow \gamma\chi_{c1}) = (3.13 \pm 0.65(stat.) \pm 0.59(syst.)) \times 10^{-3}$.
- $\mathcal{B}(J/\psi \rightarrow K_S^0 K^\pm \pi^\mp) = (2.90 \pm 0.17(stat.) \pm 0.24(syst.)) \times 10^{-3}$.

The measured branching ratios of $\psi(3770) \rightarrow \gamma\chi_{c1}$ and $J/\psi \rightarrow K_S^0 K^\pm \pi^\mp$ from this analysis and the previous results from PDG2012 [16] are summarized in Table 15. Those for $\psi(3770) \rightarrow \gamma\chi_{c1}$ are consistent with each other in consideration of statistical and systematic errors. However, those for $J/\psi \rightarrow K_S^0 K^\pm \pi^\mp$ are at odds with each other in 1σ .

Table 15: Summary of the branching ratio of $\psi(3770) \rightarrow \gamma\chi_{c1}$ from this analysis and PDG value.

Mode	Measured BF	PDG2012
$\psi(3770) \rightarrow \gamma\chi_{c1}$	$(3.13 \pm 0.65 \pm 0.59) \times 10^{-3}$	$(2.9 \pm 0.6) \times 10^{-3}$
$J/\psi \rightarrow K_S^0 K^\pm \pi^\mp$	$(2.90 \pm 0.17 \pm 0.24) \times 10^{-3}$	$\frac{1}{3}(6.1 \pm 1.0) \times 10^{-3}$

Using the PDG value $\mathcal{B}(\eta_c \rightarrow K_S^0 K^\pm \pi^\mp) = \frac{1}{3}(7.2 \pm 0.6)\%$ and the measurement from BaBar experiment $\mathcal{B}(\eta_c(2S) \rightarrow K_S^0 K^\pm \pi^\mp) = \frac{1}{3}\mathcal{B}(\eta_c(2S) \rightarrow K\bar{K}\pi) = \frac{1}{3}(1.9 \pm 0.4 \pm 1.1)\%$ [30], we can obtain:

- $\mathcal{B}(\psi(3770) \rightarrow \gamma\eta_c) < 6.9 \times 10^{-4}$ @ 90% C.L.
- $\mathcal{B}(\psi(3770) \rightarrow \gamma\eta_c(2S)) < 2.1 \times 10^{-3}$ @ 90% C.L.

Actually, this is the first measurement of these radiative transitions.

The partial width of $\psi(3770) \rightarrow \gamma\eta_c/\eta_c(2S)$ is determined by

$$\Gamma(\psi(3770) \rightarrow \gamma\eta_c/\eta_c(2S)) = \Gamma_{\psi(3770)}^{tot} \cdot \mathcal{B}(\psi(3770) \rightarrow \gamma\eta_c/\eta_c(2S)) \quad (12)$$

Inserting the measured $\mathcal{B}(\psi(3770) \rightarrow \gamma\eta_c/\eta_c(2S))$ and the world average total width $\Gamma_{\psi(3770)}^{tot}$ for $\psi(3770)$ in the above equation, we obtain the upper limits of the partial widths for $\psi(3770) \rightarrow \gamma\eta_c$ and $\psi(3770) \rightarrow \gamma\eta_c(2S)$. The comparison of measured partial widths and the theoretical predictions is summarized in Table 16.

Table 16: Summary of the measured partial widths for $\psi(3770) \rightarrow \gamma\eta_c/\eta_c(2S)$.

Mode	Measured values(Γ (keV))	IML Model(Γ (keV))
$\psi(3770) \rightarrow \gamma\eta_c$	< 18.8	$17.14^{+22.93}_{-12.03}$
$\psi(3770) \rightarrow \gamma\eta_c(2S)$	< 56.8	$1.82^{+1.95}_{-1.19}$

References

- [1] T. Appelquist, A. De Rujula, H.D. Polizer, and S.L. Glashow, Phys. Rev. Lett. **34**, 365 (1975).
- [2] S. Godfrey and N. Isgur, Phys. Rev. D **32**, 189 (1985).
- [3] T. Barnes, S. Godfrey, and E.S. Swanson, Phys. Rev. D **72**, 054026 (2005).
- [4] M. Ablikim *et al.*, BES Collaboration, Phys. Rev. D **76**, 122002 (2007).
- [5] M. Ablikim *et al.*, BES Collaboration, Phys. Lett. B **659**, 74 (2008).
- [6] M. Ablikim *et al.*, BES Collaboration, Phys. Rev. Lett. **97**, 121801 (2006).
- [7] M. Ablikim *et al.*, BES Collaboration, Phys. Lett. B **641**, 145 (2006).
- [8] G. Li and Q. Zhao, Phys. Rev. D **84**, 074005 (2011).
- [9] J.J. Dudek, R. Edwards, and D.G. Richards, Phys. Rev. D **79**, 094504 (2009).
- [10] M. Ablikim *et al.*, BESIII Collaboration, Design and construction of the BESIII detector, Nucl. Instr. Meth. A **614**, 345 (2010).
- [11] W.D. Li, H.M. Liu *et al.*, The offline software for the BESIII experiment, proceeding of CHEP06 (Mumbai, India, 13-17 February 2006).
- [12] <http://lhcb-comp.web.cern.ch/lhcb-comp/Frameworks/Gaudi/>
- [13] Z.Y. Deng *et al.*, HEP & NP, 2006, 30(5): 371-377(in Chinese).
- [14] R.G. Ping and R.L. Yang, Manual of event generators for e^+e^- scan experiments. <http://docbes3.ihep.ac.cn/DocDB/0001/000162/007/manual.pdf>
- [15] B. Aubert *et al.*, BaBar Collaboration, Phys. Rev. D **77**, 092002 (2008).
- [16] J. Beringer *et al.*, (Particle Data Group), Phys. Rev. D **86**, 010001 (2012).
- [17] M. Ablikim *et al.* BESIII Collaboration, Chinese Phys. C **37**, 123001 (2013).
- [18] E. Barberio and Z. Was, Comput. Phys. Commun. **79**, 291 (1994).
- [19] V.V. Anashin *et al.*, arXiv:1012.1694 [hep-ex].
- [20] R.E. Mitchell *et al.*, CLEO Collaboration, Phys. Rev. Lett. **102**, 011801 (2009).

- [21] C.L. Liu, G. Rong *et al.*, Study of D^0 semileptonic decays.
<http://hnb3.ihep.ac.cn/HyperNews/get/paper71.html>
- [22] M. Ablikim *et al.*, BESIII Collaboration, Phys. Rev. D **81**, 052005 (2010).
- [23] X.K. Zhou, talk on the efficiency of K_S^0 in $\psi(3770)$ at BESIII P&S Workshop on 18th Sep (2012).
- [24] T. Ma, talk on the efficiency of K_S^0 reconstruction at DQ/Validation Meeting on 8th May (2010).
- [25] M. Ablikim *et al.*, BESIII Collaboration, Phys. Rev. D **87**, 052005 (2013).
- [26] M. Ablikim *et al.*, BES Collaboration, Phys. Lett. B **650**, 111 (2007).
- [27] M. Ablikim *et al.*, BES Collaboration, Phys. Lett. B **652**, 238 (2007).
- [28] A. Vinokurova *et al.*, Belle Collaboration, Phys. Lett. B **706**, 139 (2011).
- [29] M. Benayoun *et al.*, Mod. Phys. Lett. A **14**, 2605 (1999).
- [30] B. Aubert *et al.*, BaBar Collaboration, Phys. Rev. D **78**, 012006 (2008).

Appendix

A Calculation of the ISR resonances cross sections

At first order of quantum electrodynamics (QED) the process (13):

$$e^+e^- \rightarrow \gamma V \rightarrow \gamma f, \quad (13)$$

where V is one of the vector resonances $\psi(3770)$, $\psi(3686)$, J/ψ etc. decaying to a final state f is described by two diagrams (Fig. 36). The Born term for this process can be obtained using the quasi-real electron method

$$\frac{d\sigma(s, x)}{dx d\cos\theta} = \frac{2\alpha}{\pi x} \cdot \frac{(1 - x + \frac{x^2}{2}) \sin^2 \theta}{(\sin^2 \theta + \frac{m_e^2}{E^2} \cos^2 \theta)^2} \cdot \sigma_0(s(1 - x)), \quad (14)$$

where $s = 4E^2$, E is the beam energy in the center of mass system of the electron and positron, m_e is the electron mass, α is the fine structure constant, $x = E_\gamma/E$ is the fraction of the beam energy taken by the radiative photon with the energy E_γ , θ is the photon emission angle with respect to the beam ($0 < \theta < \pi$), $\sigma_0(s)$ is the cross section of hadronic production in e^+e^- annihilation.

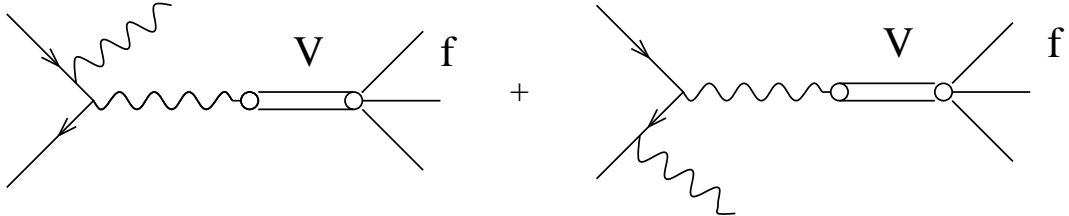


Figure 36: Main diagrams describing the process of hard photon emission.

If one performs integration over θ in (14), the following energy dependence is obtained:

$$\frac{d\sigma(s, x)}{dx} = W(s, x) \cdot \sigma_0(s(1 - x)), \quad (15)$$

where $W(s, x)$ is the probability function of the photon emission which can be written:

$$W(s, x) = \frac{2\alpha}{\pi \cdot x} \cdot (L - 1) \cdot (1 - x + \frac{x^2}{2}), \quad L = 2 \ln \frac{\sqrt{s}}{m_e} \quad (16)$$

The Born cross section of the narrow vector resonance V production is given by the standard Breit-Wigner formula

$$\sigma_0(s) = \frac{12\pi B_{ee}}{m_V^2} \cdot \frac{m_V^2 \Gamma_V^2}{(s - m_V^2)^2 + m_V^2 \Gamma_V^2}, \quad (17)$$

where m_V and Γ_V are the resonance mass and width respectively, B_{ee} is the branching fraction of the $V \rightarrow e^+e^-$ decay. If the resonance is narrow, the photon energy spectrum in reaction (13) is also narrow. The central value of the photon energy fraction is $x_V = (1 - m_V^2/s)$. For a very narrow resonance, one can replace

$$\frac{m_V \Gamma_V}{(s - m_V^2)^2 + m_V^2 \Gamma_V^2} \longrightarrow \pi \delta(s - m_V^2) \quad (18)$$

The total cross section $\sigma_V(s)$ of the process (13) can be found by the integration of (15) in the region around x_V using (17) and (18)

$$\sigma_V(s) = \frac{12\pi^2 B_{ee} \Gamma_V}{m_V \cdot s} \cdot W(s, x_V). \quad (19)$$

Assuming that the experiment is carried out at the $\psi(3770)$ energy, the production cross sections of vector mesons with quantum numbers $J^{PC} = 1^{--}$ can be calculated using (19) and PDG values for the meson masses and widths.

The cross section at first order in α has been used to estimate the main effects of hard photon emission. Equation (15) gives a correct estimate for the radiative photon emission cross section with about 10-20 % precision. Expressions which take into account the leading α^2 contributions are also well known. If we take into consideration of the leading second order correction, it would contribute up to a several percent level. Up to order α^2 , the radiator looks like

$$\begin{aligned} W(s, x) &= \Delta \cdot \beta x^{\beta-1} - \frac{\beta}{2}(2-x) + \\ &\quad \frac{\beta^2}{8} \left\{ (2-x)[3 \ln(1-x) - 4 \ln x] - 4 \frac{\ln(1-x)}{x} - 6 + x \right\}, \\ \Delta &= 1 + \frac{\alpha}{\pi} \left(\frac{3}{2}L + \frac{1}{3}\pi^2 - 2 \right) + \left(\frac{\alpha}{\pi} \right)^2 \delta_2, \\ \delta_2 &= \left(\frac{9}{8} - 2\zeta_2 \right) L^2 - \left(\frac{45}{16} - \frac{11}{2}\zeta_2 - 3\zeta_3 \right) L - \\ &\quad \frac{6}{5}\zeta_2^2 - \frac{9}{2}\zeta_3 - 6\zeta_2 \ln 2 + \frac{3}{8}\zeta_2 + \frac{57}{12}, \\ \beta &= \frac{2\alpha}{\pi}(L-1), \quad \zeta_2 = 1.64493407, \quad \zeta_3 = 1.2020569. \end{aligned} \quad (20)$$